Reducing Numerical Diffusion in Dynamical Coupling between Atmosphere and Ocean in Community Earth System Model (CESM), version 1.2.1

Jialiang Ma[1], Shiming Xu[1,3], and Bin Wang[1,2]

[1]Department of Earth System Science, Tsinghua University, Beijing, China
[2]State Key Laboratory of Numerical Modeling for Atmospheric Sciences and Geophysical Fluid Dynamics (LASG), Institute of Atmospheric Physics, Chinese Academy of Sciences, Beijing, China
[3]University Corporation for Polar Research, Beijing, China

Key Points:

- The dynamical coupling in CESM is improved to reduce the numerical diffusion in dynamics-physics coupling in the atmospheric component.
- Improvements in SST are attained for upwelling regions and Southern Oceans, by direct interpolation for atmospheric winds from dynamic core.
- The new scheme can be applied to other models with staggered dynamic core and physics parameterization.

Corresponding author: Shiming Xu, xusm@tsinghua.edu.cn

Abstract

Climate models contain atmospheric and oceanic components that are coupled together to simulate the thermodynamic and dynamic processes during air-sea interactions. Community Earth System Model (CESM, version 1.2.1) is a state-of-the-art coupled model that is widely used and participates in Coupled Model Intercomparison Projects. Community Atmospheric Model (CAM), the atmospheric component of CESM, is based on the finite-volume dynamic core, which utilizes staggered Arakawa-D grids. However, the dynamics-physics (D-P) coupling in CAM causes the prognostic winds of the dynamic core be interpolated onto non-staggered locations, which affects the wind structure for computing the air-sea interaction and dynamical coupling. In this study we propose a new scheme that eliminates the extra interpolation during D-P coupling for the atmosphere-ocean interaction. By numerical experiments and comparative study of the new scheme, we show that it improves the simulated climatology in key regions including eastern-boundary upwelling regions and Southern Oceans. In turn, existing problems of the model, such as warm SST biases, are reduced. The new scheme contain code changes in CAM and the coupler, and they are provided as open-source files. Similar approaches can also be adopted in coupled models that utilize the atmospheric components with on staggered dynamics and physics, such as spectral-element method based CAM.

Plain Language Summary

Coupled models simulate air-sea interaction by coupling components models together. However, in state-of-the-art models such as CESM, the atmospheric model contains dynamic core and physic parameterization that are not differentiated during air-sea interaction. We propose a new dynamical coupling scheme specific for Finite-Volume version of the atmospheric component in CESM. Model biases in key regions are reduced with the new scheme, including upwelling regions and sea ice modeling in the Southern Oceans. The scheme can be applied to other models to better exploit the dynamic core's capability by reducing the numerical diffusion during the dynamics-physics coupling for air-sea interactions.

1 Introduction

Background of AO coupling in climate models

Coupled models are indispensable tools for climate studies (Flato et al., 2013) and key applications such as operational forecasts (Jia et al., 2015). State of the art coupled models, including those participating in Coupled Model Intercomparison Projects (WCRP-CMIP, 2019, accessed 2019-Dec-31), usually consist of component models of atmospheric general circulation models (AGCM) and oceanic general circulation models (OGCM). Common to coupled models are also other components including land surface model, sea ice model, biogeochemistry processes, etc. Due to the sheer complexity of these component models, they are usually: (1) developed independently, and (2) coupled together in an on-line fashion. The dynamical and thermodynamical processes during air-sea interaction are usually carried out by flux couplers (Craig et al., 2012) through the computation of boundary processes and the exchange of momentum and tracer fluxes. Usually, the atmospheric and oceanic components adopt different spatial discretization and grids, and the sea ice component adopts the same grid as the oceanic component. Therefore, the flux coupler is also responsible for the spatial and temporal interpolation of fluxes between the them.

CESM

Community Earth System Model (CESM) is a state-of-the-art coupled climate model developed at National Center for Atmospheric Research (NCAR). It couples component models to carry out climate simulations, and it actively participates in Coupled Model Intercomparison Projects. In this study, we use CESM version 1.2.1 (Hurrell et al., 2013)

for analysis and model improvements. The major component models of CESM includes: the Community Atmosphere Model version 4 (CAM4) (Neale et al., 2013), with a finite-volume (FV) dynamical core (Lin, 2004), the Parallel Ocean Program version 2 (POP2) (Smith et al., 2010; Danabasoglu et al., 2012), Community Land Model version 4 (CLM4) (Oleson et al., 2015) and Community Ice Code version 4 (CICE4) (Hunke & Lipscomb, 2008). The components are coupled by the flux coupler CPL7 (Craig et al., 2012). For CESM version 1.2.1, CPL7 is in charge of the execution and time evolution of the component models, communicates interfacial states and fluxes between components and carries out mapping flux and other calculations. Due to the computational burden of high-resolution models, CESM based CMIP experiments are mainly based on 1° resolution settings, which is typical among models participating in CMIP.

Grid staggering & Interpolation

In coupled models such as CESM, both the atmospheric and the ocean component consist of dynamic core for resolvable fluid dynamics and physical parameterizations that deal with unresolved processes. As is common in finite difference (or finite difference-finite volume) method based models, the dynamic core is constructed on structured grids, with prognostic variables defined on staggered locations on the grid (Arakawa & Lamb, 1977). The grid staggering usually differentiates between velocities and state variables, and it improves the effective spatial resolution of the dynamic core. Physics parameterization, on the contrary, are usually carried out on non-staggered grid locations. For example, CAM adopts Finite Volume dynamic core (Lin, 2004) with Arakawa-D grid staggering in the horizontal direction. CAM also contains a dynamic core based on spectral-element (SE) method (Dennis et al., 2005) which enables high-precision and flexible modeling (X. Huang et al., 2016). Recently, Herrington et al. (2019) introduced similar grid staggering between the SE dynamic core and a quasi-equal-area physics parameterization scheme. Therefore, the exists a general interpolation process between the dynamics and the parameterization in atmospheric models such as CAM. The coupling between CAM and the oceanic and sea ice component in CESM is carried out for state variable, fluxes, and atmospheric winds by separate processes. For the dynamic coupling (i.e., the atmospheric winds), the process involving interpolations are shown in Figure 1. The interpolation of wind vectors from the FV dynamic core is carried out from D-points to A-points (U/V_AD $\rightarrow$ U/V_AA). After the tendencies by the physics parameterizations are added to the winds (through "Physics Run1"), the wind vectors on the A-points are passed to the coupler, which carries out another interpolation process to map the winds onto the oceanic component's grid. As is shown in Zarzycki et al. (2016), the interpolation grid during the dynamic coupling can play an important role in simulating key phenomenon of tropical cyclones.

Paper outline

In this paper we propose an improvement to the dynamic coupling process between the atmospheric and the oceanic component in CESM. Since the prognostic variables of atmospheric winds by the dynamic core of CAM-FV is defined on D-points of the Arakawa grid, the interpolation process during the dynamics-physics transition inherently introduces numerical diffusion to the wind field and its structure. Potentially this downgrades the effective resolution of wind fields for the oceanic component. The new coupling scheme exploits the atmospheric winds from the dynamic core and the effects on winds from physics schemes, by differentiating them during the dynamic coupling process. In the following up part of the paper, in Section 2, we introduce the details of CESM and its component models, and the design and implementation of the new coupling scheme. In Section 3, we show the benefit of the new scheme through numerical experiments based on CMIP and analysis of two typical regions for air-sea interaction. Further, Section 4 summarizes the article, and provides discussion of potential application in future developments of coupled models including CESM.

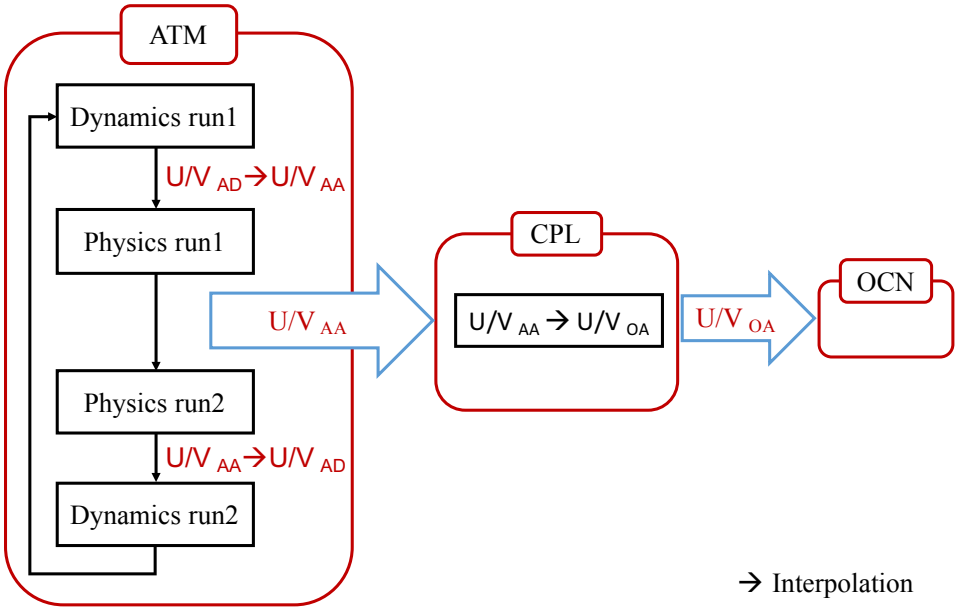

Figure 1. Dynamical coupling of CAM-FV and POP in CESM.

2 Atmosphere-ocean dynamical coupling in CESM

2.1 CESM and atmosphere-ocean dynamic coupling

In this study we adopt NCAR CESM version 1.2.1, and use the atmospheric component CAM-FV (Lin, 2004), the oceanic component POP2 (Danabasoglu et al., 2012), and the sea ice component of CICE version 4 (Hunke & Lipscomb, 2010). The dynamic core of CAM-FV is based on the latitude-longitude grid, and carries out discretization and numerical integration of the hydrostatic approximation of the atmospheric circulation with a finite-volume framework. In specific, the spatial discretization and prognostic variable layout of CAM-FV is on the Arakawa D-grid (Arakawa & Lamb, 1977), with atmospheric winds located on the north/south (for U-wind) and east/west (for V-wind) staggered locations. We use AD to denote the D-points of the D-grid of CAM-FV. Physics parameterization schemes of CAM-FV include deep-shallow convection, clouds, gravity wave drag, etc. These schemes, together with the dynamics-physics (D-P) coupling, are carried on the A-grid, which denote as AA (Fig. 2.a). The D-P coupling involves interpolation of prognostic wind velocities from Arakawa-D to Arakawa-A points at each time step. After physical parameterization computation on A-grid, the tendencies to prognostic variables (including wind vectors) are added, and the final prognostic wind variables, state variables and fluxes are passed to CPL7 for coupling. After coupling, the second half of the physics schemes and dynamic core computation are carried out, including: vertical diffusion, Rayleigh friction, gravity wave drag, etc. On the other hand, POP2 utilizes Arakawa-B grid and a general orthogonal global grid, which is different from the Lat-Lon grid of CAM-FV. Therefore, the exchange of (tracer and momentum) fluxes, the air-sea interaction, is carried out between CAM-FV and POP2 through an interpolation process. Specifically, the interpolated wind vector is targeted at the cell center locations of the oceanic model's grid (denoted OA). For the coupling between CAM-FV and CICE in polar regions, since in CESM CICE and POP2 utilize the same grid, the interpolation and the inherent dynamical coupling between CAM-FV and CICE is the same as that between CAM-FV and POP2. For CESM, various coupling variables are treated differently: (1) for state variables, such as temperature, it is carried out with a bi-linear interpolator; (2) for fluxes, such as sensible and latent heat, a conservative in-

terpolator is adopted; (3) for the dynamical coupling, i.e., for atmospheric winds, a high-order interpolator based on local recovery based on patches is adopted.

A typical scenario of dynamical coupling between CAM-FV and POP2 (or CICE4 when ice is present) is illustrated in Fig. 2.a. State variables and tracers of CAM-FV are located at the centers of the red cell (ATM-AA: red circle points) whereas the horizontal velocity U and V of the dynamic core are located at the south/north and west/east edges of the cell (ATM-AD: red cross points), respectively. Centers of the cells (ATM-AA) are also where the physics parameterization is carried out, and in the model, they cast the influence by adding a physical tendencies to the prognostic variables, including surface winds. Before coupling to the ocean, the winds on the bottom level of CAM-FV defined on the A-point contains two parts: (1) the winds interpolated from the dynamic core, and (2) the physical tendency to the winds from the physical parameterization. Then, these winds are passed to the coupler, which carries out the boundary layer computation and passed to the ocean and sea ice components (Fig. 1 and 2.a).

2.2 Improved coupling scheme

To remove extra interpolation of dynamic core to physical space and associated numerical diffusion, we try to decouple dynamics-physics process in CAM-FV as follows. The improved atmosphere-ocean dynamical coupling scheme is shown in Figure 3. The main changes are in CAM-FV and CPL7. In CAM-FV, the original interpolation of prognostic winds from ATM-AD grid to ATM-AA grid in first dynamics-physics coupling and interpolation from ATM-AA grid to ATM-AD grid in second dynamics-physics couple process are kept the same. The difference from the original scheme is that the addition between prognostic winds U/V and physical tendencies $\Delta U/V$ is no longer applied. Meanwhile the physical tendencies of wind on ATM-AA grid produced by physical parameterization are also recorded, and together with wind vectors on ATM-AD grid they are all passed to coupler. From the atmosphere-ocean coupling's perspective, CPL is responsible for two parts of work. First, U/V_{AD} and $\Delta U/V_{AA}$ are interpolated from atmosphere ATM-AD grid and ATM-AA grid to ocean OCN-OA grid, respectively. Second, the interpolation results are added together to compute the final wind vectors on ocean OCN-OA grid. In short, when coupling wind vectors from atmosphere to ocean in original CAM-FV scheme, prognostic winds on ATM-AD grid are generally interpolated to ATM-AA grid, then remapped to ocean OCN-OA (shown as Fig. 2.a). The new scheme, as shown in Fig. 2.b with bilinear interpolator, eliminates the extra interpolation during D-P coupling within CAM-FV. Therefore, wind vectors are interpolated directly from ATM-AD grid to OCN-OA grid without through ATM-AA grid. For the sake of simplicity, Fig. 2 demonstrate the scheme with bilinear interpolations. In CESM, patch recovery method is utilized for mapping wind vectors, in which about 20 nearby vector points in CAM-FV are used for the interpolation to each ocean grid location. For the new scheme, since U-wind and V-wind reside on different geophysical locations, two independent and different interpolators are constructed with patch recovery method.

2.3 Model configuration and implementation details

For CESM (version 1.2.1), we use standard configuration of CAM-FV with $0.9^\circ \times 1.25^\circ$ resolution (F09) and POP2/CICE4 with 1° nominal resolution (GX1V6) for implementation and test. For CAM-FV, the model contains 26 vertical levels. For POP2 and CICE, the model grid is a dipolar grid with the north pole shifted onto Greenland, and the grid has 60 vertical layers. This resolution configuration is also used by NCAR for CMIP experiments, including CMIP5 and CMIP6.

In order to support the new dynamic coupling scheme, modifications to the atmospheric component (CAM-FV) and coupler (CPL7) are made to the CESM codebase. In specific, the following changes are carried out. It is worth to note that the code changes

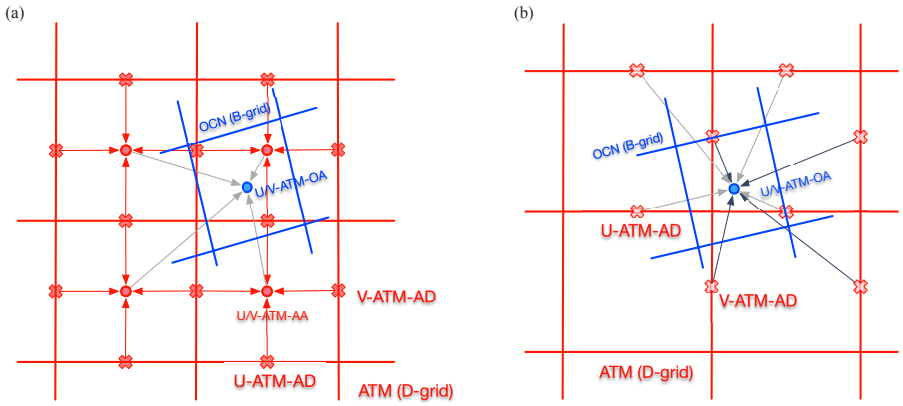

Figure 2. Schematics of atmosphere-ocean dynamical coupling scheme: (a) original scheme; (b) new scheme in which only the interpolation of winds from the dynamic core is shown. Bilinear interpolation is shown for the sake of simplicity.

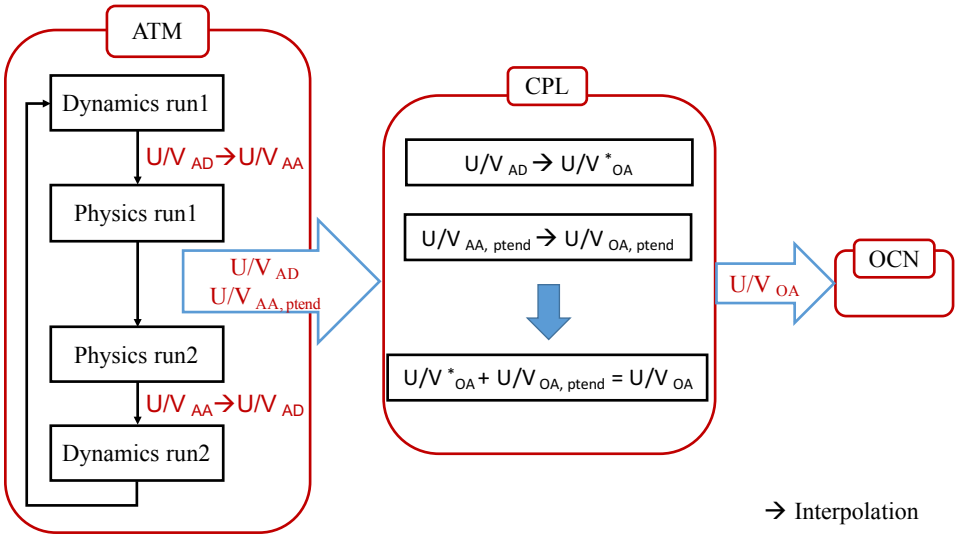

Figure 3. Improved atmosphere-ocean dynamical coupling scheme in CESM.

Table 1. Model and experiments

Experiment	Atmosphere model	Ocean model	Description
F09	CAM-FV ($0.9° \times 1.25°$)	POP ($\sim 1°$)	Pre-Industrial Control run, initializes from steady state, and integrates for 100 years.
Mod_cp	CAM-FV ($0.9° \times 1.25°$)	POP ($\sim 1°$)	Same as F09, but with the new ATM-OCN dynamic coupling scheme.

are specific to CAM-FV, and not limited to this resolution configuration. Also, for the interpolation of $\Delta U/V$ from the ATM-AA grid to OCN-A grid, the original interpolators are still used.

1. In CAM-FV, new definitions of variables that record: (1) U/V_{AD} (on ATM-AD grid) and (2) $\Delta U/V$ (on ATM-AA grid);
2. During coupling, the variables above are passed to CPL7;
3. In CPL7, two new interpolation operators are defined, in order to carry out the interpolation of U/V_{AD} onto the ocean's grid;
4. In CPL7, the codes are added for the interpolation of all the 4 variables (U/V_{AD} and $\Delta U/V$) and the addition to produce the final atmospheric wind vector that is passed to the ocean component.

The code changes include in total 9 FORTRAN files and 4 configuration files in the existing codebase. They are provided in open-source format, as attachments to this article. The new interpolators for U/V_{AD} between FCAM-FV (F09) and POP2/CICE4 (G16) are also provided as standard interpolator data files. Furthermore, we carried out consistency tests of the implementation. The new scheme guarantees perfect restart, with the exemption of new restart states.

3 Experiments and evaluation

Two comparative CESM experiments are carried out, as shown in Table 1. They are both fully coupled simulations, based on pre-industrial (piControl) forcing in CMIP5 (Taylor et al., 2012). Under piControl, the climatic forcings are fixed at the level of year 1850, including greenhouse gases, ozone, aerosols and solar irradiance. This experiment is usually used to evaluate and study the equilibrium state and climatology of the coupled model. For the two experiments in this study, the model configurations of both atmospheric and oceanic components are aligned, with the only difference being the new interpolation scheme. We use F09 to denote the experiment with the original scheme, and Mop_cp the new one. The resolution and grid settings are F09 and G16 respectively, which is typical of climate simulations. F09 and Mod_cp are typical piControl runs: the model is initialized from a steady state, and integrated for 100 years under pre-industrial forcings. in order to eliminate the effect of spin-up, we use the last 50 years of results for analysis.

We mainly use three datasets for the validation of the simulation results. In order to align with the pre-industrial forcings, the climatologies for each dataset are adopted for further validations. The first dataset is the Sea Surface Temperature (SST) observational dataset in Hurrell et al. (2008). The data merges monthly mean Hadley Centre sea ice and SST dataset version 1 (HadISST1) and the National Oceanic and Atmo-

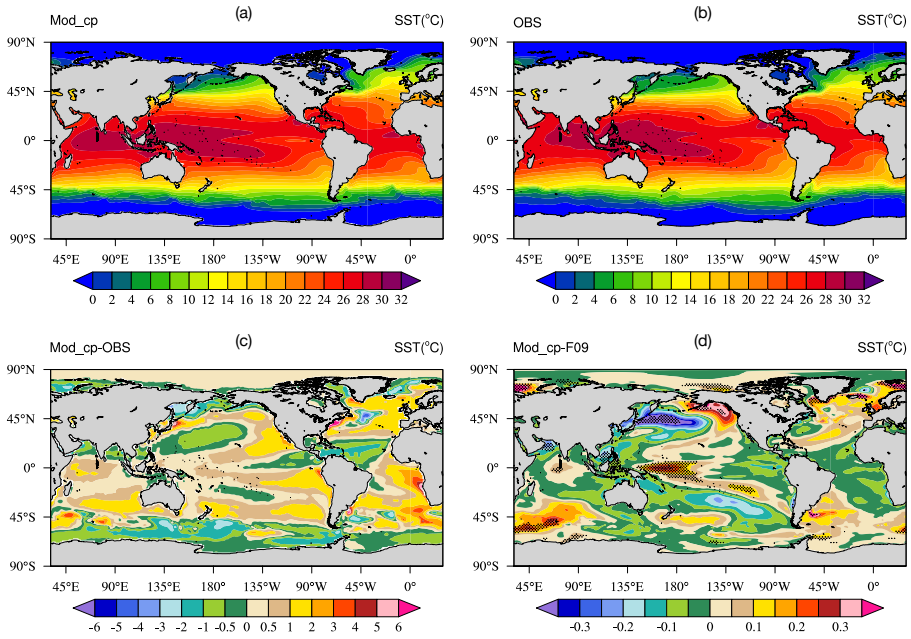

Figure 4. SST in Mod_cp (a) and comparison with climatological SST in Hurrell et al. (2008) (b). Difference between Mod_cp and climatology is shown in panel c, and that between Mod_cp and F09 in panel d. 50 years of simulation after spin-up is used to compute the statistical significant changes in SST in Mod_cp as compared with F09 (dotted in panel d).

spheric Administration weekly optimum interpolation SST version 2 (OISST V2). The merged Hadley-OI SST and sea ice concentration data sets were specifically developed as the surface forcing data for AMIP simulations of the CAM model. We use it as the climatological record for comparison with pre-industrial runs with the original and the new scheme in CESM. The second dataset is National Centers for Environmental Prediction (NCEP) Climate Forecast System Reanalysis (CFSR) (Saha et al., 2010). The NCEP/CFSR is a global, high-resolution, fully-coupled ocean-atmosphere system with coupled assimilation, and it provides the estimation of dynamics and thermodynamics of both atmosphere and ocean. The horizontal resolution of the CFSR atmospheric component is about 38 km. Specifically, we use the monthly wind stress fields during 1979-2008 for the comparison of our experiments. Third, we use the monthly sea ice concentration (SIC) fields provided by National Snow and Ice Data Center (NSIDC), which are produced from passive microwave satellite remote sensing by Scanning Multi-channel Microwave Radiometer (SMMR) and Special Sensor Microwave Imager (SMMI) (Stroeve & Meier, 2018). The monthly SIC fields from 1979 to 2000 are used to produce a climatological annual cycle of sea ice concentration.

Figure 4 shows the multi-year annual mean sea-surface temperature (SST) fields of Mod_cp and the differences against climatology and F09. Overall, in Mod_cp, a reasonable global SST is attained. Compared with climatology, the most prominent SST biases for Mod_cp is present in the following regions: (1) in Southern Oceans there is prevalent cold bias; (2) in Western Boundary Currents (WBC) and their extensions, there is cold and warm biases caused by the specific location path and separation of WBCs; (3) in eastern boundary regions the warm biases manifest for both Pacific Ocean and Atlantic Ocean. These features in biases are in alignment with existing studies with CESM (Gent et al., 2010). The new scheme simulates different climatology than the original

scheme (panel d), with prominent differences in the following regions. First, in the southeast basin of the Pacific and Atlantic Ocean, the new scheme simulates colder SST, which compensates with the warm bias in these regions. Second, to contrast, the new scheme simulates a warmer warm pool. Third, in the Northern Pacific, a see-saw pattern of SST difference emerges, which is similar to both the observational Pacific Decadal Oscillation (PDO) pattern and that simulated by CESM. This may be due to the limited length of 50 years for fully analyze the PDO due to the long period of PDO and the ensuing difference in PDO phases of these two simulations. Lastly, in the Southern Oceans, the new scheme generally reduces the SST bias.

We further examine the effect of the new scheme on two regions with representative dynamical coupling processes. They are: (1) Eastern Boundary Upwelling Systems (EBUS), and (2) Southern Oceans (SO). EBUS are located at the eastern boundaries of the tropical and subtropical oceans, and they are charactered by strong upwelling process driven by alongshore prevailing wind. Upwelling systems bring cold nutrient-rich deep water to the ocean surface, leading to the formation of cooling and high biological productivity area. The physical process in EBUS is extremely sensible to alongshore wind structure and strength. They are biologically productive marine regions, covering less than 2% of the global ocean surface but providing 7% global marine primary production and almost 20% world's fish catches (Pauly & Christensen, 1995). There exists characteristic wind pattern so-called wind drop-off in the zonal direction across the sea-land boundary. The meridional wind strength gradually increases when approaching land-sea boundary, then decreases abruptly at the proximity of land due to land-sea contrast and land topography. The Southern Ocean is referred to the ocean from the coast of Antarctica to south of subtropical convergence (about $40°S$). The Antarctic Circumpolar Current (ACC) circulates in the clockwise direction, from west to east around Antarctic, which is the dominant circulation feature of SO. ACC is a coupled phenomenon, and it is mainly driven by strong westerly winds in SO. Meanwhile, there exists easterly winds forcing the ocean in a much narrower band around Antarctic coast. The clockwise westerlies in mid latitude and narrow counterclockwise easterlies around near-Antarctic form meridional gradient of wind speed. Also, the sea ice cover in SO features a pronounced annual cycle, of which the dynamic and thermodynamic processes are also driven by atmospheric wind and oceanic response. Therefore, we further examine the simulation of these regions with the new scheme, and contrast with the original scheme. Section 3.1 and 3.2 includes the specific results for these two regions, respectively.

3.1 Eastern boundary upwelling regions

There are four main EBUS systems in the globe, including California Current System, Canary Current System, Humboldt Current System and Benguela Current System. However, most coupled general circulation models (CGCMs) suffer from warm SST biases in these systems and westward extension ocean areas (Richter & Xie, 2008; Zheng et al., 2011; Wang et al., 2014; Xu, Chang, et al., 2014; Toniazzo & Woolnough, 2014; Richter, 2015; J. Ma et al., 2019). CESM simulations also show large warm biases in EBUS regions, especially in Southeast Pacific (SEP) and Southeast Atlantic (SEA). As shown in Figure 5.a, there exists maximum warm SST bias up to 6 $°C$ around 17.5 $°S$ in SEA, and over 2 $°C$ in SEP alongshore region.

A large body of existing studies have been investigating the origin of these biases, and many models contain common problems, including CESM. Causes of bias mainly come from different dynamic and thermodynamic processes of ocean and atmosphere component. From the ocean's perspective, model resolution is regarded as one of the major limits. Wahl et al. (2011) concluded that underestimation of presentation of ocean upwelling system was caused by the low resolution of ocean models. Meanwhile, low resolution ocean model is reported to be unable to simulate the process of eddies that transport cold water from coast to the open ocean, resulting in warmer SST and larger bias

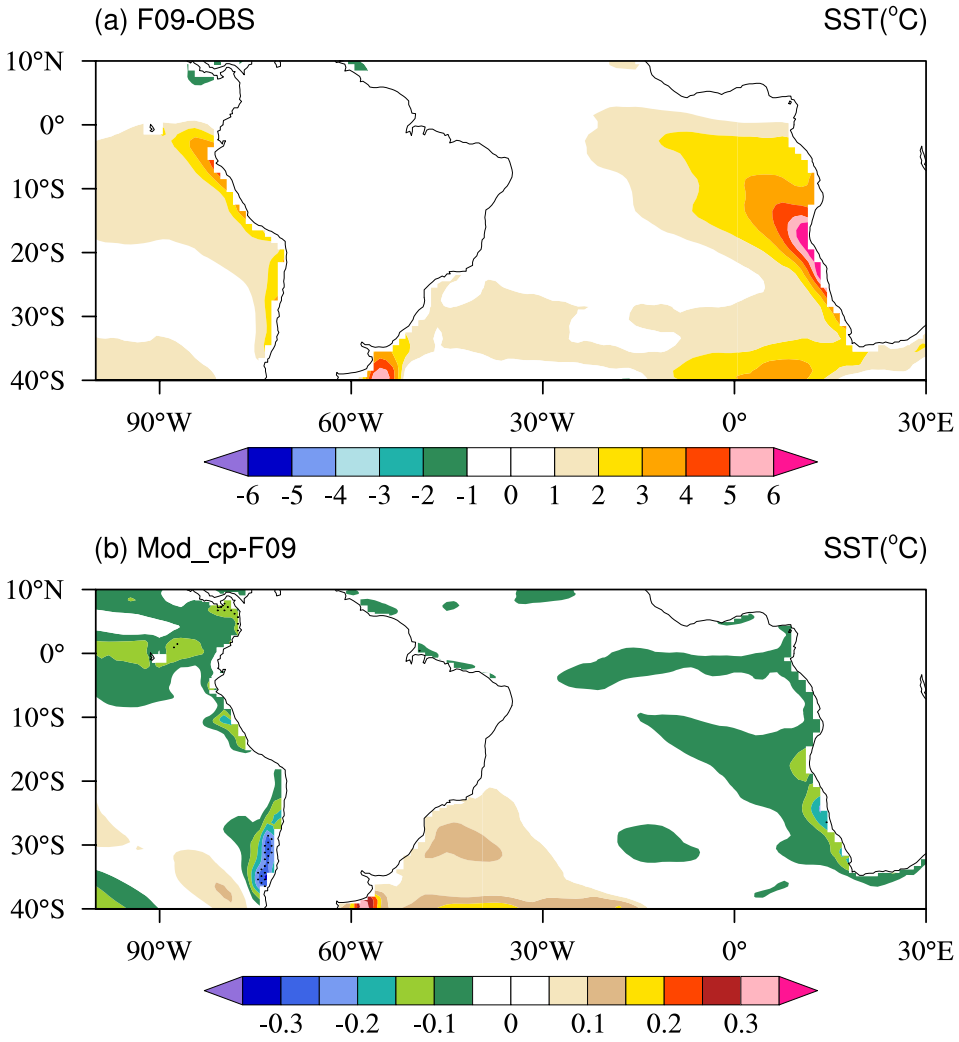

Figure 5. Sea Surface Temperature difference: (a) between CESM F09 and Hadley; (b) between Mod_cp and F09. Black dots indicate that the difference is statistically significant at 0.05 significance level.

in this region (Colbo & Weller, 2007). Xu, Li, et al. (2014) suggested oceanic origin of southeast tropical Atlantic bias make a significant contribution to warm bias. For example, the equator-ward Benguela current and poleward Angola current meet between 15 $^{\circ}S$ and 17 $^{\circ}S$ in southeast tropical Atlantic, forming the Angola-Benguela Font (ABF) (Mohrholz et al., 2001; Shannon et al., 1987). However, modeled ABF position is always located more southward due to the overshooting of Angola current, which has large contribution to warm bias here.

From the atmosphere's perspective, excessive solar radiation into the ocean due to underestimation of stratocumulus decks is widely considered a major cause of SST warm biases in EBUS (C.-C. Ma et al., 1996; B. Huang et al., 2007; Hu et al., 2008). However, some other studies reveal complex cases within this general argument. First, the shortwave radiation errors were overcompensated for by larger errors of upward surface longwave radiation and turbulent heat fluxes (De Szoeke et al., 2010; Xu, Chang, et al., 2014; Toniazzo & Woolnough, 2014; Richter, 2015). Second, the solar radiation bias was too small to generate such large SST biases (Large & Danabasoglu, 2006; Wahl et al., 2011). The low cloud bias and stratocumulus-SST feedback only partially explain the bias, so the coastal upwelling process may have more contribution to the SST bias especially close to shore. Besides, coastal upwelling is extremely sensitive to the strength and structure of alongshore wind. First, downwind coastal currents could be generated by alongshore wind (Philander & Yoon, 1982). Second, Ekman offshore currents are generated when nearshore prevailing wind is equatorward, then the deep cold water is upwelled to make up of the divergence of nearshore surface water. Further, negative wind stress due to wind drop-off structure is responsible for the Ekman pumping-driven upwelling. Last but not least, Small et al. (2015) pointed out when negative wind stress is too broad, the Sverdrup balance prevails in EBUS, implying more southward transport of equatorial warm water.

However, the simulated alongshore wind by CGCMs tends to be much weaker in EBUS. Comparison of modeled wind stress of CESM and CFSR reanalysis is illustrated in Fig. 6.a and b. It is evident that the wind stress shows more north wind bias nearshore, which indicates that the north wind part of subtropical gyre is much smaller alongshore. In particular, the maximum low-level jet deficiency is located at around 30 $^{\circ}S$ of SEP, 15 $^{\circ}S$ and 27.5 $^{\circ}S$ of SEA, where the maxima of observational wind stress cores are. The results are also consistent with other existing modeling study of wind structures in these regions. In Patricola and Chang (2017), the authors compared the structure and strength of Benguela low-level coastal jet (LLCJ) from observations, reanalyses and atmospheric model simulations. The conclusion was that the LLCJ is characterized by two near-shore maxima of SEA region in finer resolution products and models, including satellite-based SCOW and CCMP, atmospheric reanalyses such as CFSR, and regional climate model simulation at 9, 27 and 81 km resolution. For comparison, modeled maximum wind stress in CESM is far from coast, resulting in weaker upwelling response nearshore. Maximum wind stress is located much closer to the coast at finer atmosphere component of Community Climate System Model, leading to increase of coastal upwelling and reduction of SST (Gent et al., 2010; Small et al., 2015). However, most atmosphere components of CGCMs (e.g. those in CMIP5) have coarse resolution (coarser than about 2 $^{\circ}$), resulting in poor representation of wind stress and consequent ocean response. These warm biases are also present in ocean general circulation models (OGCMs) forcing by prescribed atmosphere. Not only the ocean systematic errors in ocean models, but also the quality of forcing wind plays important role. Small et al. (2015) showed more realistic representation of upwelling system by adopting the 0.5 $^{\circ}$ atmosphere model wind structure near the coast toward observations. To summarize, the structure of surface wind stress and wind stress curl plays a critical role in coastal upwelling and SST pattern in EBUS.

The surface atmospheric wind structure and the ocean's response is inherently a dynamical coupling process. With the new coupling scheme, the warm bias is reduced

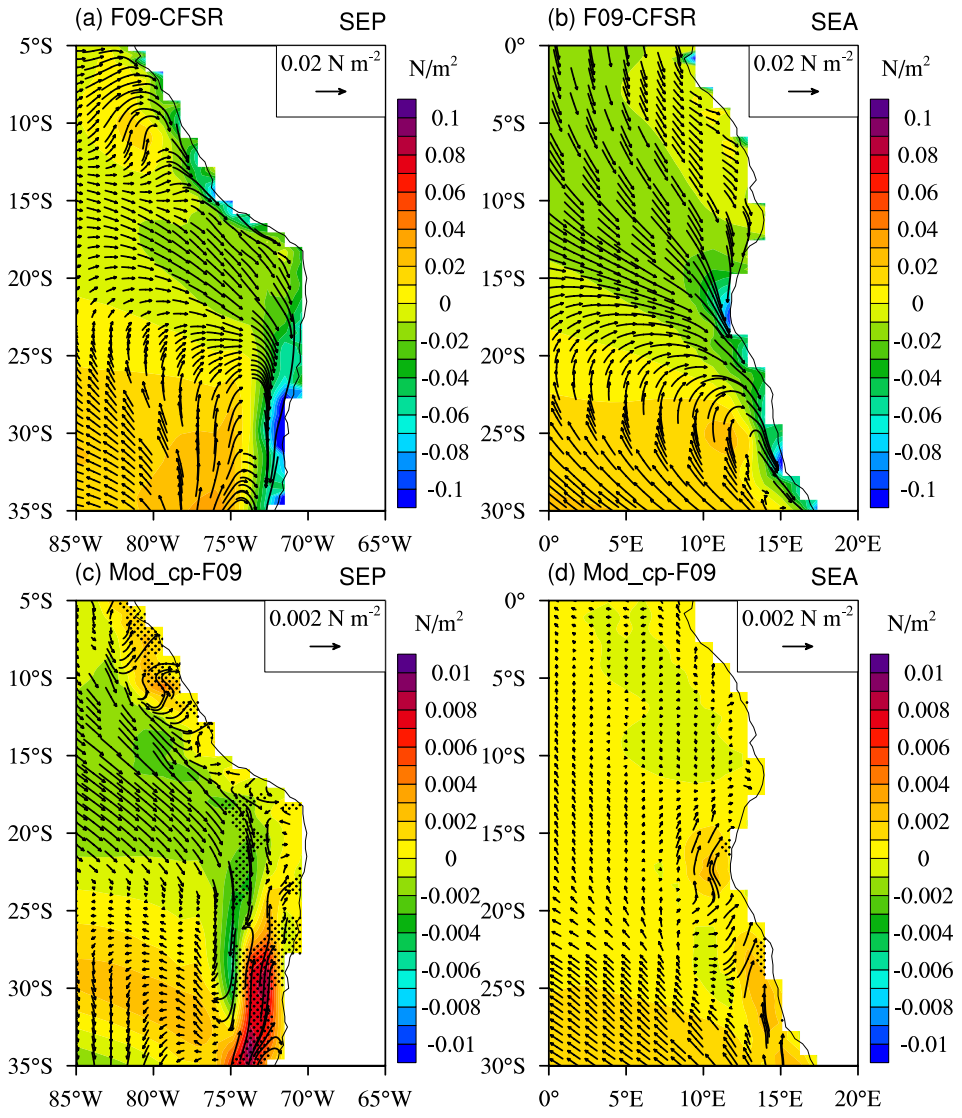

Figure 6. Wind stress bias of F09 relative to CFSR reanalysis: (a) Southeast Pacific region, (b) Southeast Atlantic region; Wind stress difference between Mod_cp and F09: (c) SEP region, (d) SEA region. Black dots indicate that the difference is statistically significant at 0.05 significance level.

by 5% $\sim$ 15% in EBUS, compared with the original coupling scheme (Fig. 5.b). The attribution shows that the new scheme improves the simulation of wind structure and strength. With the new scheme, the coastal low-level jet in these regions are improved in strength. As shown in Fig. 6.c and d, the maximum wind stress is more equator-ward and closer to the coast, bringing wind stress curl larger nearshore. The increased wind stress and wind stress curl nearshore could bring more cold water reaching this region in horizontal and vertical direction, respectively. As a result, the ocean responds both dynamically and thermodynamically. Fig. 7 shows the difference of ocean subsurface meridional and vertical velocity between the new scheme and original one. Thereinto, meridional velocity is averaged of 2.5 ° away from coast, from 35 °S to 5 °S. With the new scheme, more cold subsurface water is transported towards the equator from the south (Fig. 7.a and b). Vertical velocity is calculated at the latitude 30 °S of SEP and 17.5 °S of SEA, where the maximum wind cores are located. As shown, more cold water are upwelled from deep ocean to nearshore surface (Fig. 7.c and d).

3.2 Effects on Southern Oceans and sea ice

The Southern Ocean occupies about 20% area of the world's ocean, if the region is extended to the south of subtropical convergence. SO is charactered by the strongest wind in the world (Wunsch, 1998) and large seasonal range of sea ice coverage (Cavalieri & Parkinson, 2008; Thomas & Dieckmann, 2008). However, there are two major problems in representation of the SO in CESM (version 1.2.1). Weijer et al. (2012) suggested the main characteristic of CCSM4 simulation was a significant cold bias with respect to observations in the Antarctic surface waters. Second, the ice extent of CCSM4 is too extensive throughout the year compared to satellite observations (Landrum et al., 2012). Fig. 8.a shows the climatological mean SMMR/SMMI ice extent (black solid line) and simulated ice area difference between new coupling scheme experiment and original one in CESM.

Compared with the original coupling scheme, the new scheme shows reduction of ice coverage, especially in the East Atlantic, Indian ocean and East Pacific at nearby 60°S latitude. As a result, sea surface temperature cold bias is reduced due to the disappearance of sea ice in these regions as a response (Fig. 8.b). With Mod_cp, both the circumpolar westerlies and easterly wind exist in a much narrower meridional band around Antarctic coast (Fig. 9.a). To the quantify the increase, area averaged zonal wind stress growth rate is calculated in the westerlies region (62.5 °S $\sim$ 50 °S) and easterlies area (about 1 ° band width around Antarctic). As shown in Tab. 2, westerlies of ocean component increased by 2.94% in new coupling scheme, and easterlies increased by 1.65%. Meanwhile, the most significant increase is present in Atlantic, Indian ocean and East Pacific at about 60 °S, which is also the area of largest sea ice extent decrease. The result implies the relationship between the increase of wind stress strength and the decrease of sea ice extent. For further breakdown the contribution of new interpolation method to the wind stress increase, the growth rate of atmosphere zonal wind at bottom level is also calculated (shown as Fig. 9.b). The growth rate pattern of bottom zonal wind is similar, but not as significant as that of zonal wind stress. The area averaged zonal westerly wind of bottom level itself increases by 1.59%. The difference between growth rate of westerly wind at bottom level and zonal westerly wind stress is attributed to new coupling process: where the modeled westerlies manifest, the interpolation contributes about 1.33% to the 2.94% increase in zonal ocean wind stress. Meanwhile, zonal easterly wind at bottom level shows no intensification, which is contrary to the growth rate pattern of ocean easterly wind stress. As a result, the growth rate of zonal wind at atmosphere bottom level is negative, and interpolation process contributes 3.74% to the ocean zonal wind stress. In all, the increase of zonal wind stress is mainly determined by the new interpolation process. As a response to the westerlies increase, mixed layer is deepened (Fig. 9.c).

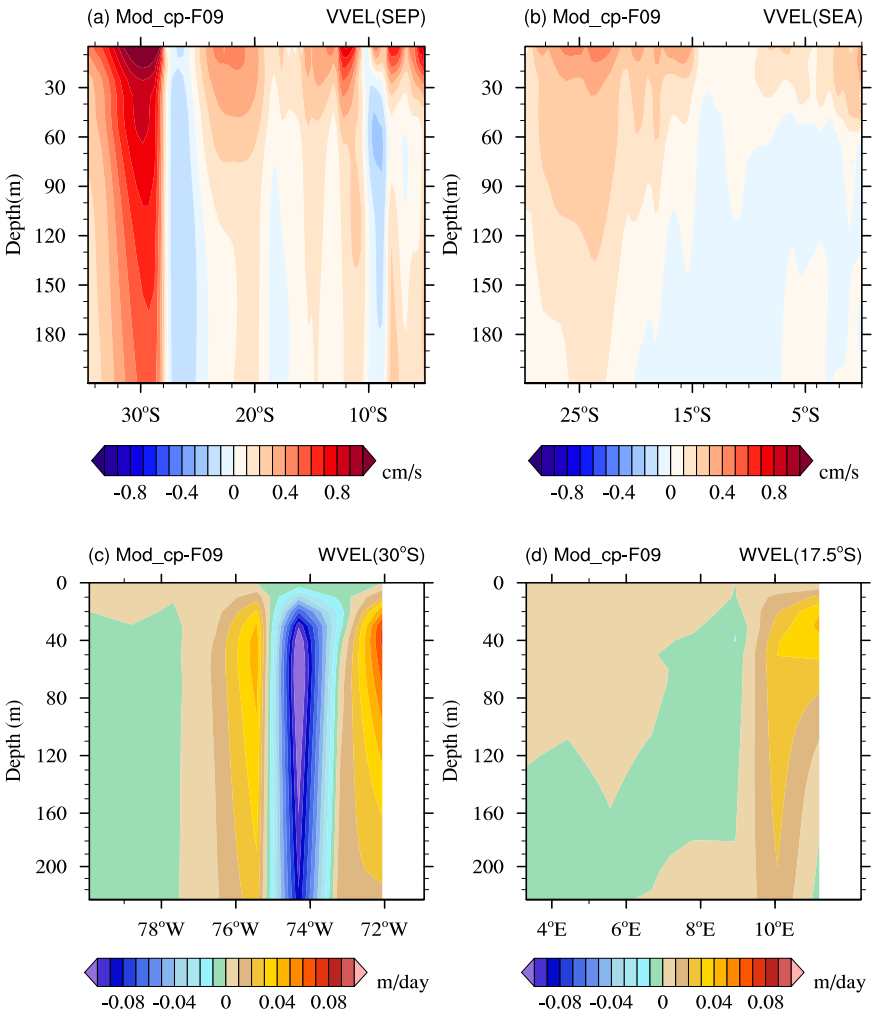

Figure 7. Ocean response to wind stress and wind stress curl. The difference of meridional and vertical velocity between new dynamical coupling scheme and original one. Meridional velocity is averaged at the region of 2.5 degree away from coast in (a) Southeast Pacific, (b) Southeast Atlantic region; Vertical velocity-longitude cross-section is at the latitude (c) $30°S$ of SEP region and (d) $17.5°S$ of SEA region.

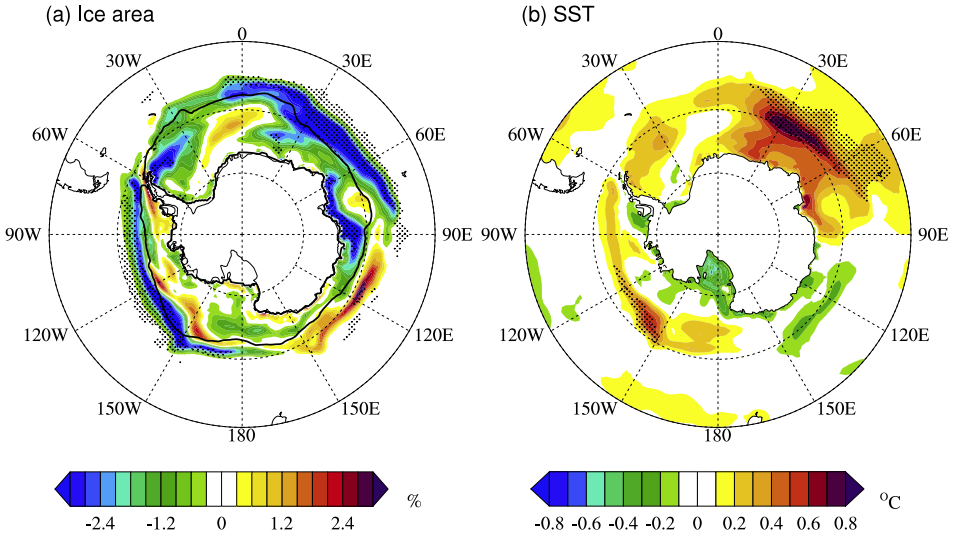

Figure 8. The difference of (a) sea ice area and (b) sea surface temperature between new dynamical coupling and original one. Black dots indicate that the difference is statistically significant at 0.05 significance level.

Table 2. Growth rate of wind in Southern Ocean.

Index	Westerlies ($62.5°S$-$50°S$)	Easterlies ($1°$ band north of Antarctic)
Zonal wind at ATM bottom level	1.59%	-2.01%
Zonal wind stress of ocean	2.94%	1.65%
Contribution of interpolation	1.33%	3.74%

The Antarctic Circumpolar Current is dominated by the circumpolar westerlies. As a consequence, more sea ice tends to be transported to lower latitude. The evidence in Fig. 10 shows the difference of zonal averaged ice volume tendency owing to dynamics and thermodynamics effects, comparing new dynamical coupling scheme with the original one. As shown, the ice decreases at higher latitude (south of about 70 $°S$), and increases at lower latitude due to dynamic effect. Nevertheless, the ice melts due to higher solar radiation and more available ocean heat at lower latitudes. As the overall effect of dynamic and thermodynamic response, ice extent decreases both in higher and lower latitudes of Southern Ocean (illustrated as black solid line in Fig. 10). Meridional ice transport difference of two schemes provides evidence for above conclusion (purple marked line in Fig. 10). The meridional transport south of 67.5 $°S$ is most pronounced. However, ice transport tendency north of 67.5 $°S$ is in effect decreased, which is mainly due to thermodynamic loss of the overall ice volume budget.

4 Summary and discussion

Summary

In this article we propose a new dynamical coupling scheme for CESM. By utilizing the dynamics-physics (D-P) coupling in the atmospheric component of CAM-FV, we reduce the numerical diffusion in the air-sea dynamical coupling by differentiate the contribution by the dynamic core and physics parameterizations. The new scheme helps to

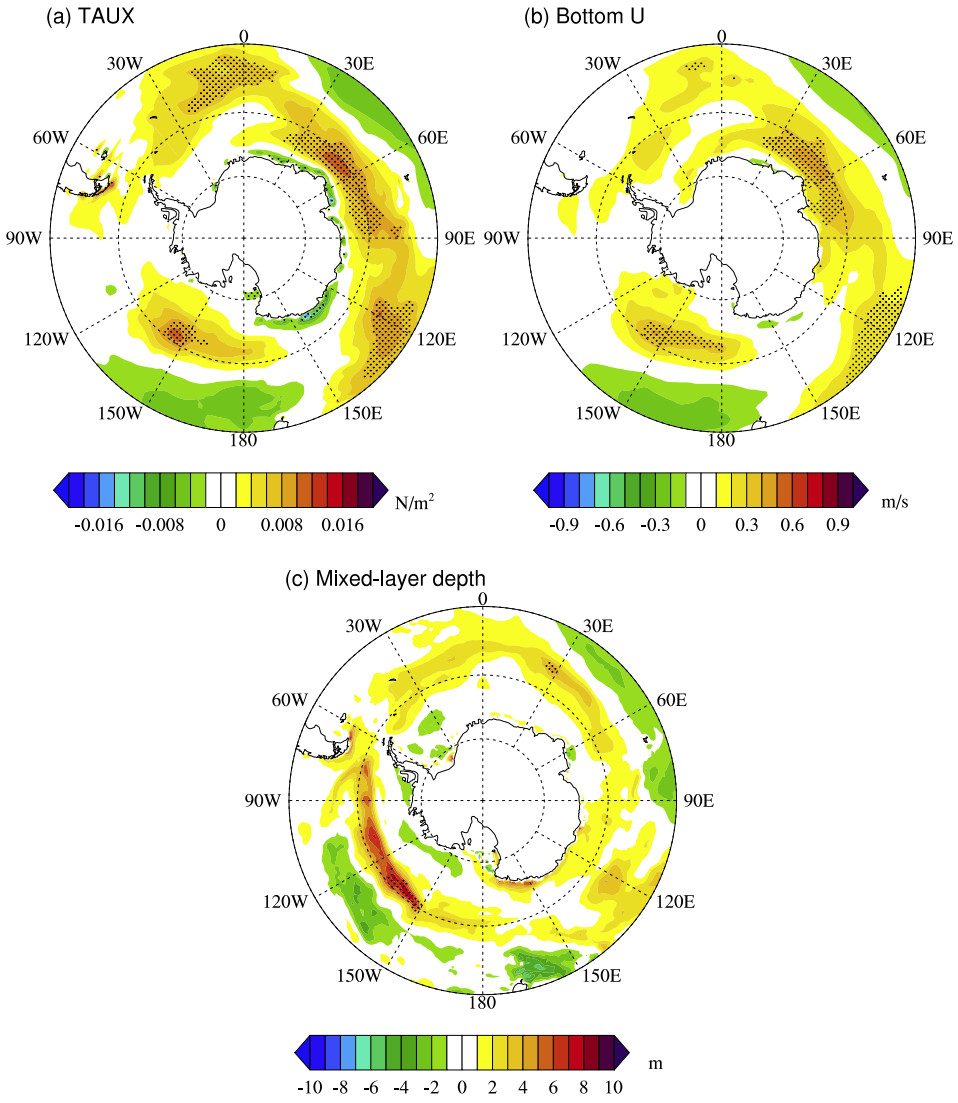

Figure 9. Difference between Mod_cp and F09 for (a) ocean zonal wind stress, (b) zonal wind speed of atmosphere bottom level, and (c) mixed layer depth in SO. Black dots indicate that the difference is statistically significant at 0.05 significance level.

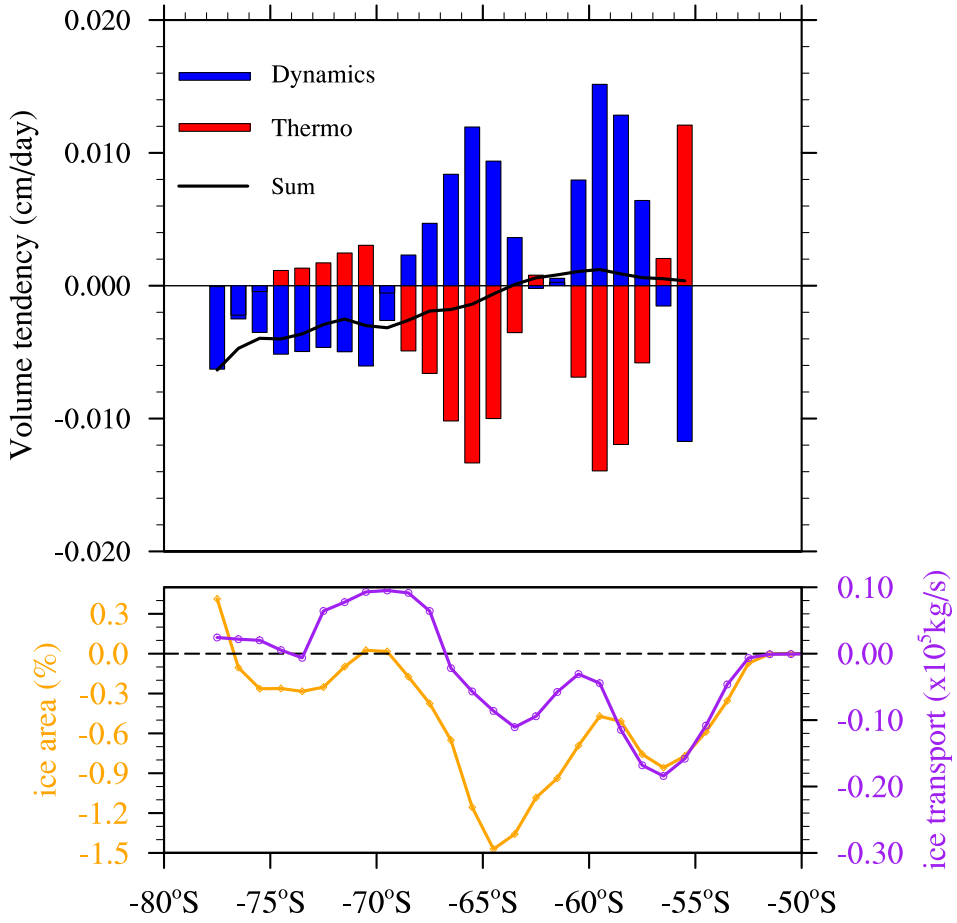

Figure 10. Zonal mean sea ice volume tendency difference between Mod_cp and F09 due to dynamics (blue bar), thermodynamics (red bar) and the combined effect (black solid line). The difference of sea ice area (orange marked line) and meridional ice transport (purple marked line) between Mod_cp and F09 is shown in the lower panel.

improve the wind structure for typical regions with dynamical coupling. Specifically, in eastern upwelling regions in the eastern Pacific and Atlantic ocean, the wind and wind drop-off is enhanced for the ocean, with For Southern Oceans where the atmosphere and sea ice interaction is present, the new scheme promotes more meridional sea ice transport and results in more effective sea ice melt at lower latitudes. Consequently, the overestimation of sea ice extent and negative bias in SST is reduced. On the computational perspective, the new scheme only introduces extra variables during the coupling process, and no extra computation is involved. Therefore, the new scheme doe not affect the simulation speed of the model.

General applicability

Atmospheric models all contain dynamic core, physics parameterizations, and D-P coupling, and many of them contain staggered grid settings (Lin, 2004; Herrington et al., 2019). Therefore, the methodology proposed in this study can also be applied to other CESM configurations or other coupled models. For example, the dynamic core of CAM-SE utilizes 4rd-order spectral-element algorithm and spatial discretization based on Gauss-Lobatto-Legendre (GLL) quadrature grid. In Herrington et al. (2019) the quasi-equal-area physics parameterization scheme is designed to accompany the CAM-SE dynamic core, in order to reduce spurious numerical noises on the GLL grid. The scheme we proposed in this study can be applied accordingly as follows. The prognostic atmospheric (U and V) winds from the SE dynamic core (both defined on collocating points on the GLL grid) and the physics tendencies of the winds (defined on the equal-area grid) can be treated independently with a separate interpolation process.

Open-source usage

For the proposed scheme on coupling CAM-FV and POP2 (or CICE) in CESM (version 1.2.1), we provide the updated source files of the codebase on GitHub (downloadable at: `https://github.com/gongbell/Improved-AO-Coupling-in-CESM`). A brief guide is also provided at the site for code changes and incorporation in existing codebases. Besides, simple revisions of the code can be applied for adoptions in other versions of CESM. For the 0.9° CAM-FV model (F09) and its coupling with the 1° POP2 (i.e., GX1V6), we also provide the data files of the interpolators (from D-points on F09 grid to GX1V6 A-points). The interpolators are based on patch-recovery algorithm, and generated from ESMF utilities (available at `https://www.earthsystemcog.org/projects/esmf/`). The source files and associated interpolator data files have been subjected to long-term pre-industrial experiments and model restart tests for their validity.

Future work

In this study we have demonstrated that the new scheme attains model improvements in typical regions, by improving air-sea dynamical coupling and reducing known model biases. Further, more systematic analysis is needed in future studies, in order to evaluate its effect in simulating the global and regional climatology and climate variability. Especially, for the two regions as examined in this study, the following works are planned. For EUBC regions, two aspects of the SST warm bias are noted. First, although the new scheme attains certain reduction of the warm bias, the improvement is comparatively small compared with high resolution, 0.5 ° simulations in the atmospheric component (J. Ma et al., 2019; Gent et al., 2010), although there is large increase in computational overhead with these runs. Second, the simulation of stratocumulus cloud decks over the open ocean in SEP is not improved. Therefore, in order to overcome the SST biases in EUBC regions, a more systematic solution is needed to improve both wind structure and cloud simulations. For sea ice in both Southern Oceans and the Arctic, since the atmosphere is the main driver of the ice drift and kinematics, the effect of the new scheme on sea ice circulation and response to climate change is planned as future work.

Acknowledgments

The authors would like to express sincere thanks to the editor and referees for the invaluable efforts in helping improve the manuscript. This work is partially support by National Key R & D Program of China: [Grant Number 2017YFA0603902] and the National Science Foundation of China: [Grant Number 41575076]. This work is also partially supported by Center for High Performance Computing and System Simulation, Pilot National Laboratory for Marine Science and Technology (Qingdao).

We gratefully acknowledge Hurrell et al. (2008)'s work of merging Hadley-OI sea surface temperature and sea-ice concentration (available at `ftp://ftp.cgd.ucar.edu/archive/SSTICE`), NCEP CFSR group (available at `https://rda.ucar.edu/datasets/ds093.2/`) and NSIDC (dataset at `https://nsidc.org/data/nsidc-0192`), for providing public access to the observational and reanalysis data sets. The source code of the scheme is available at github.com at: `https://github.com/gongbell/Improved-A0-Coupling-in-CESM`.

References

Arakawa, A., & Lamb, V. R. (1977). Computational design of the basic dynamical processes of the UCLA general circulation model. *General circulation models of the atmosphere*, *17*(Supplement C), 173–265.

Cavalieri, D., & Parkinson, C. (2008). Antarctic sea ice variability and trends, 1979–2006. *Journal of Geophysical Research: Oceans*, *113*(C7).

Colbo, K., & Weller, R. (2007). The variability and heat budget of the upper ocean under the Chile-Peru stratus. *Journal of Marine Research*, *65*(5), 607–637.

Craig, A. P., Vertenstein, M., & Jacob, R. (2012). A new flexible coupler for earth system modeling developed for CCSM4 and CESM1. *The International Journal of High Performance Computing Applications*, *26*(1), 31–42.

Danabasoglu, G., Bates, S. C., Briegleb, B. P., Jayne, S. R., Jochum, M., Large, W. G., ... Yeager, S. G. (2012). The CCSM4 ocean component. *Journal of Climate*, *25*(5), 1361-1389.

Dennis, J., Fournier, A., Spotz, W., St-Cyr, A., Taylor, M., Thomas, & et al. (2005). High resolution mesh convergence properties and parallel efficiency of a spectral element atmospheric dynamical core. *International Journal of High Performance Computing Applications*, *19*, 225-235.

De Szoeke, S. P., Fairall, C. W., Wolfe, D. E., Bariteau, L., & Zuidema, P. (2010). Surface flux observations on the southeastern tropical Pacific ocean and attribution of SST errors in coupled ocean–atmosphere models. *Journal of Climate*, *23*(15), 4152–4174.

Flato, G., Marotzke, J., Abiodun, B., Braconnot, P., Chou, S., Collins, W., ... Rummukainen, M. (2013). Evaluation of climate models. In T. Stocker et al. (Eds.), *Climate change 2013: The physical science basis. contribution of working group i to the fifth assessment report of the intergovernmental panel on climate change* (p. 741-866). Cambridge, United Kingdom and New York, NY, USA: Cambridge University Press.

Gent, P. R., Yeager, S. G., Neale, R. B., Levis, S., & Bailey, D. A. (2010). Improvements in a half degree atmosphere/land version of the CCSM. *Climate Dynamics*, *34*(6), 819–833.

Herrington, A. R., Lauritzen, P. H., Taylor, M. A., Goldhaber, S., Eaton, B. E., Bacmeister, J. T., ... Ullrich, P. A. (2019). Physics-dynamics coupling with element-based high-order Galerkin methods: quasi equal-area physics grid. *Monthly Weather Review*, *147*, 69-84. doi: 10.1175/MWR-D-18-0136.1

Hu, Z.-Z., Huang, B., & Pegion, K. (2008). Low cloud errors over the southeastern Atlantic in the NCEP CFS and their association with lower-tropospheric stability and air-sea interaction. *Journal of Geophysical Research: Atmospheres*,

113(D12).

Huang, B., Hu, Z.-Z., & Jha, B. (2007). Evolution of model systematic errors in the tropical Atlantic basin from coupled climate hindcasts. *Climate dynamics*, *28*(7-8), 661–682.

Huang, X., Rhoades, A. M., Ullrich, P. A., & Zarzycki, C. M. (2016). An evaluation of the variable-resolution CESM for modeling California's climate. *Journal of Advances in Modeling Earth Systems*, *8*. doi: 10.1002/2015MS000559

Hunke, E. C., & Lipscomb, W. H. (2008). CICE: The Los Alamos sea ice model documentation and software user's manual version 4.0 LA-CC-06-012. In *Version 4.0, la-cc-06-012, Los Alamos National Laboratory.*

Hunke, E. C., & Lipscomb, W. H. (2010). *CICE: the Los Alamos sea ice model documentation and software user's manual version 4.1* (Tech. Rep. No. LA-CC-06-012). Los Alamos National Laboratory.

Hurrell, J. W., Hack, J. J., Shea, D., Caron, J. M., & Rosinski, J. (2008). A new sea surface temperature and sea ice boundary dataset for the Community Atmosphere Model. *Journal of Climate*, *21*(19), 5145–5153.

Hurrell, J. W., Holland, M. M., Gent, P. R., Ghan, S., Kay, J. E., Kushner, P. J., ... Lindsay, K. (2013). The Community Earth System Model: A framework for collaborative research. *Bulletin of the American Meteorological Society*, *94*(9), 1339-1360.

Jia, L., Yang, X., Vecchi, G. A., Gudgel, R. G., Delworth, T. L., Rosati, A., ... Dixon, K. (2015). Improved seasonal prediction of temperature and precipitation over land in a high-resolution gfdl climate model. *Journal of Climate*, *28*(5), 2044-2062. doi: 10.1175/JCLI-D-14-00112.1

Landrum, L., Holland, M. M., Schneider, D. P., & Hunke, E. (2012). Antarctic sea ice climatology, variability, and late twentieth-century change in CCSM4. *Journal of Climate*, *25*(14), 4817–4838.

Large, W., & Danabasoglu, G. (2006). Attribution and impacts of upper-ocean biases in CCSM3. *Journal of Climate*, *19*(11), 2325–2346.

Lin, S.-J. (2004). A vertically Lagrangian finite-volume dynamical core for global models. *Monthly Weather Review*, *132*(10), 2293–2307.

Ma, C.-C., Mechoso, C. R., Robertson, A. W., & Arakawa, A. (1996). Peruvian stratus clouds and the tropical Pacific circulation: A coupled ocean-atmosphere GCM study. *Journal of Climate*, *9*(7), 1635–1645.

Ma, J., Xu, S., & Wang, B. (2019). Warm bias of sea surface temperature in eastern boundary current regions - a study of effects of horizontal resolution in CESM. *Ocean Dynamics*, *69*, 939-954. doi: 10.1007/s10236-019-01280-4

Mohrholz, V., Schmidt, M., & Lutjeharms, J. (2001). The hydrography and dynamics of the Angola-Benguela frontal zone and environment in April 1999: BENEFIT marine science. *South African Journal of Science*, *97*(5-6), 199–208.

Neale, R. B., Richter, J., Park, S., Lauritzen, P. H., Vavrus, S. J., Rasch, P. J., & Zhang, M. (2013). The mean climate of the community atmosphere model (CAM4) in forced SST and fully coupled experiments. *Journal of Climate*, *26*(14), 5150-5168.

Oleson, K. W., Niu, G. ., Yang, Z. ., Lawrence, D. M., Thornton, P. E., Lawrence, P. J., ... Levis, S. (2015). Improvements to the Community Land model and their impact on the hydrological cycle. *Journal of Geophysical Research Biogeosciences*, *113*(G1), G01021.

Patricola, C. M., & Chang, P. (2017). Structure and dynamics of the Benguela low-level coastal jet. *Climate Dynamics*, *49*(7-8), 2765–2788.

Pauly, D., & Christensen, V. (1995). Primary production required to sustain global fisheries. *Nature*, *374*(6519), 255.

Philander, S., & Yoon, J. (1982). Eastern boundary currents and coastal upwelling. *Journal of Physical Oceanography*, *12*(8), 862–879.

Richter, I. (2015). Climate model biases in the eastern tropical oceans: Causes, impacts and ways forward. *Wiley Interdisciplinary Reviews Climate Change*, *6*(3), 345-358.

Richter, I., & Xie, S.-P. (2008). On the origin of equatorial Atlantic biases in coupled general circulation models. *Climate Dynamics*, *31*(5), 587–598.

Saha, S., Moorthi, S., Pan, H.-L., Wu, X., Wang, J., Nadiga, S., ... others (2010). The NCEP climate forecast system reanalysis. *Bulletin of the American Meteorological Society*, *91*(8), 1015–1058.

Shannon, L., Agenbag, J., & Buys, M. (1987). Large-and mesoscale features of the Angola-Benguela front. *South African Journal of Marine Science*, *5*(1), 11–34.

Small, R. J., Curchitser, E., Hedstrom, K., Kauffman, B., & Large, W. G. (2015). The Benguela upwelling system: Quantifying the sensitivity to resolution and coastal wind representation in a global climate model. *Journal of Climate*, *28*(23), 9409–9432.

Smith, R., Jones, P., Briegleb, B., Bryan, F., Danabasoglu, G., Dennis, J., ... others (2010). The parallel ocean program (POP) reference manual: ocean component of the community climate system model (CCSM) and community earth system model (CESM). *Rep. LAUR-01853*, *141*, 1–140.

Stroeve, J., & Meier, W. (2018). Sea ice trends and climatologies from SMMR and SSM/ISSMIS, version 3. *Sea Ice Extent. Boulder, Colorado USA. NASA National Snow and Ice Data Center Distributed Active Archive Center. doi: https://doi. org/10. 5067/IJ0T7HFHB9Y6*.

Taylor, K. E., Stouffer, R. J., & Meehl, G. A. (2012). An overview of CMIP5 and the experiment design. *Bulletin of the American Meteorological Society*, *93*(4), 485–498.

Thomas, D. N., & Dieckmann, G. S. (2008). *Sea ice: an introduction to its physics, chemistry, biology and geology*. John Wiley & Sons.

Toniazzo, T., & Woolnough, S. (2014). Development of warm SST errors in the southern tropical Atlantic in CMIP5 decadal hindcasts. *Climate dynamics*, *43*(11), 2889–2913.

Wahl, S., Latif, M., Park, W., & Keenlyside, N. (2011). On the tropical Atlantic SST warm bias in the Kiel climate model. *Climate Dynamics*, *36*(5-6), 891–906.

Wang, C., Zhang, L., Lee, S. K., Wu, L., & Mechoso, C. R. (2014). A global perspective on CMIP5 climate model biases. *Nature Climate Change*(3), 201-205.

WCRP-CMIP. (2019, accessed 2019-Dec-31). *Wcrp coupled model intercomparison project.* Retrieved from `https://www.wcrp-climate.org/wgcm-cmip`

Weijer, W., Sloyan, B. M., Maltrud, M. E., Jeffery, N., Hecht, M. W., Hartin, C. A., ... Landrum, L. (2012). The southern ocean and its climate in CCSM4. *Journal of Climate*, *25*(8), 2652–2675.

Wunsch, C. (1998). The work done by the wind on the oceanic general circulation. *Journal of Physical Oceanography*, *28*(11), 2332–2340.

Xu, Z., Chang, P., Richter, I., & Tang, G. (2014). Diagnosing southeast tropical Atlantic SST and ocean circulation biases in the CMIP5 ensemble. *Climate dynamics*, *43*(11), 3123–3145.

Xu, Z., Li, M., Patricola, C. M., & Chang, P. (2014). Oceanic origin of southeast tropical Atlantic biases. *Climate dynamics*, *43*(11), 2915–2930.

Zarzycki, C. M., Reed, K. A., Bacmeister, J. T., Craig, A. P., Bates, S. C., & Rosenbloom, N. A. (2016). Impact of surface coupling grids on tropical cyclone extremes in high-resolution atmospheric simulations. *Geoscientific Model Development*, *9*, 779-788. doi: 10.5194/gmd-9-779-2016

Zheng, Y., Shinoda, T., Lin, J.-L., & Kiladis, G. N. (2011). Sea surface temperature biases under the stratus cloud deck in the southeast Pacific ocean in 19 IPCC AR4 coupled general circulation models. *Journal of Climate*, *24*(15),

4139–4164.

Figure1.

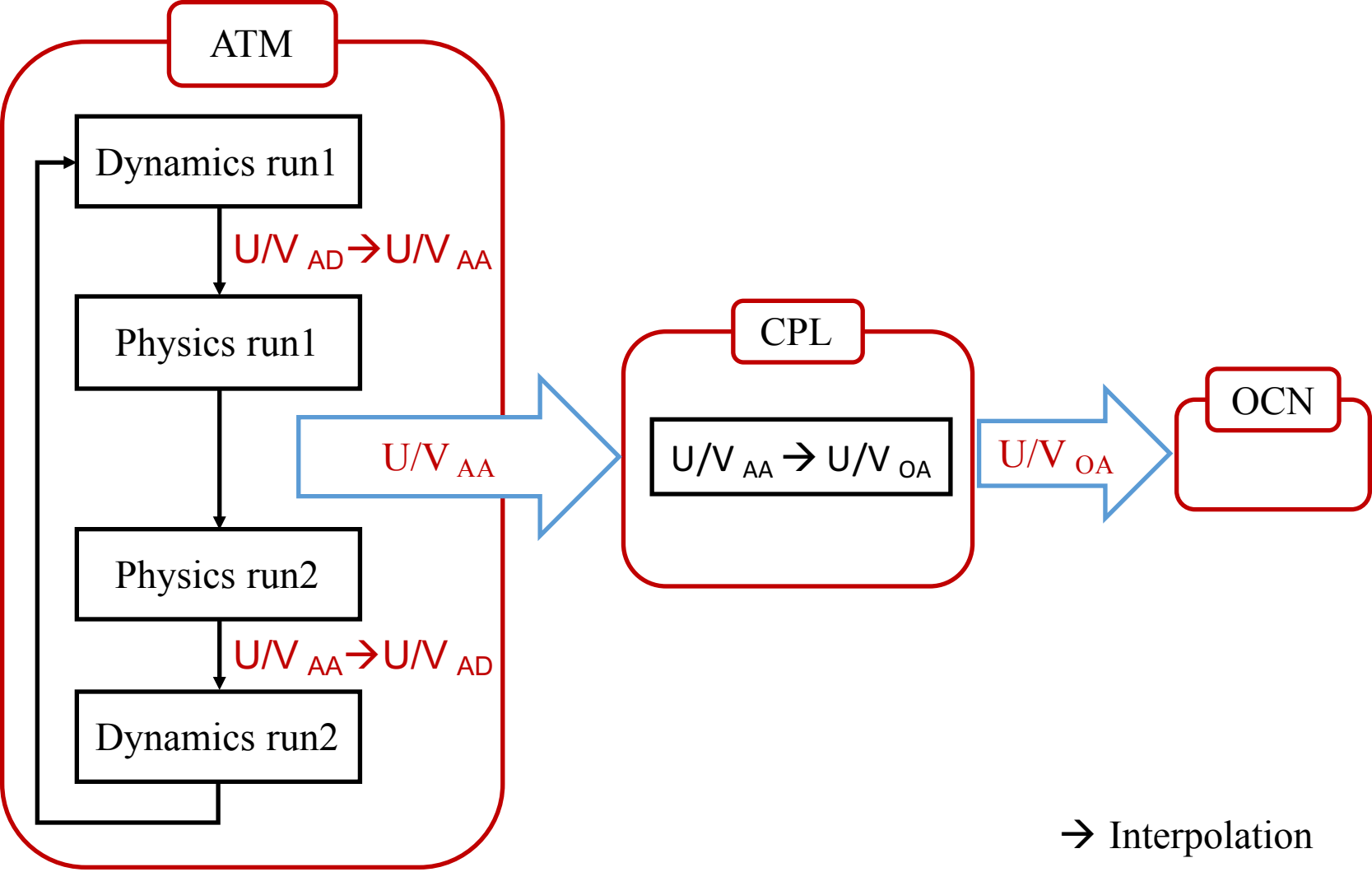
ATM
Dynamics run1
U/V AD→U/V AA
Physics run1
Physics run2
U/V AA→U/V AD
Dynamics run2
U/V AA
CPL
U/V AA → U/V OA
U/V OA
OCN
→ Interpolation

Figure2.

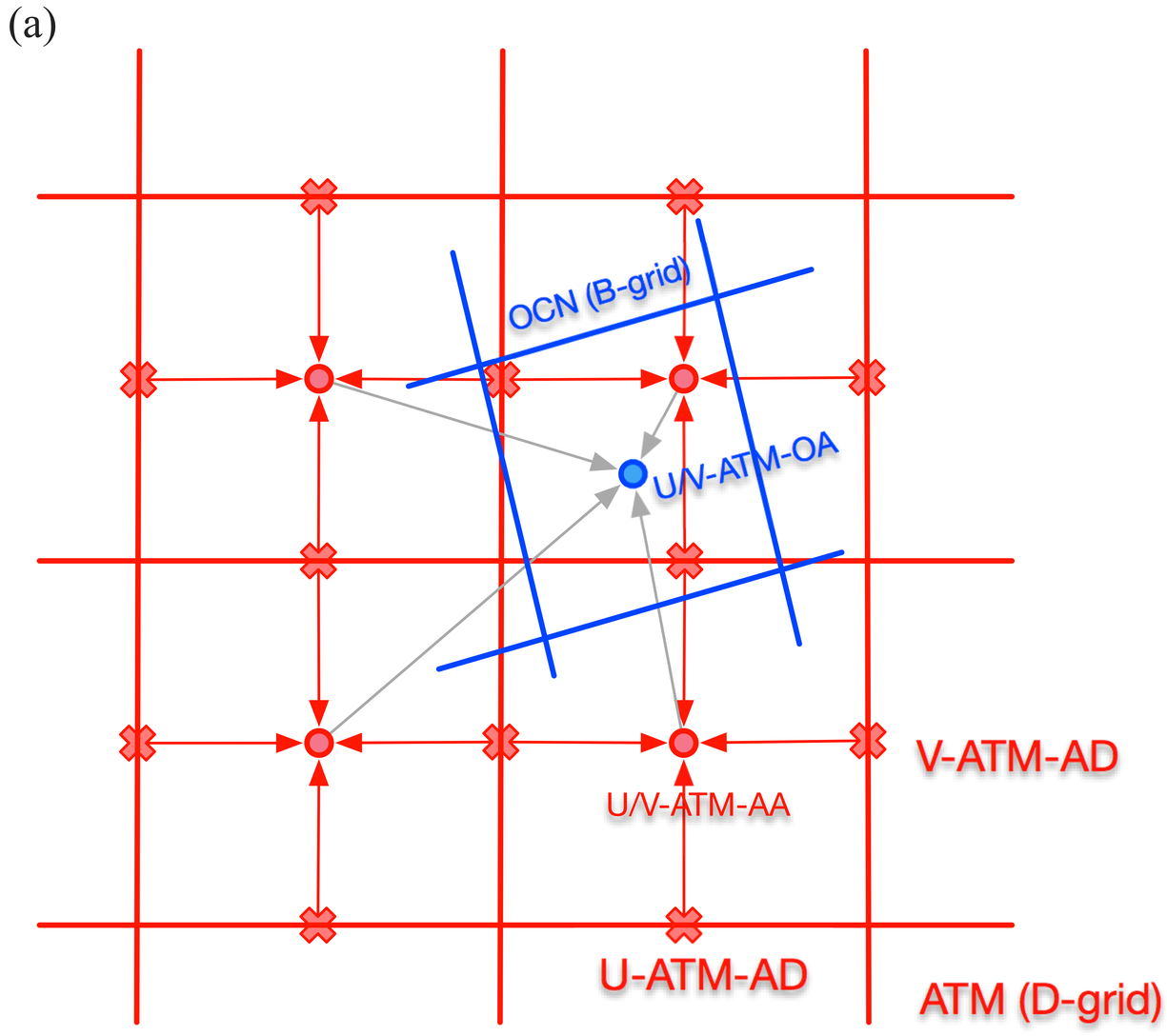
(a)
OCN (B-grid)
U/V-ATM-OA
U/V-ATM-AA
V-ATM-AD
U-ATM-AD
ATM (D-grid)

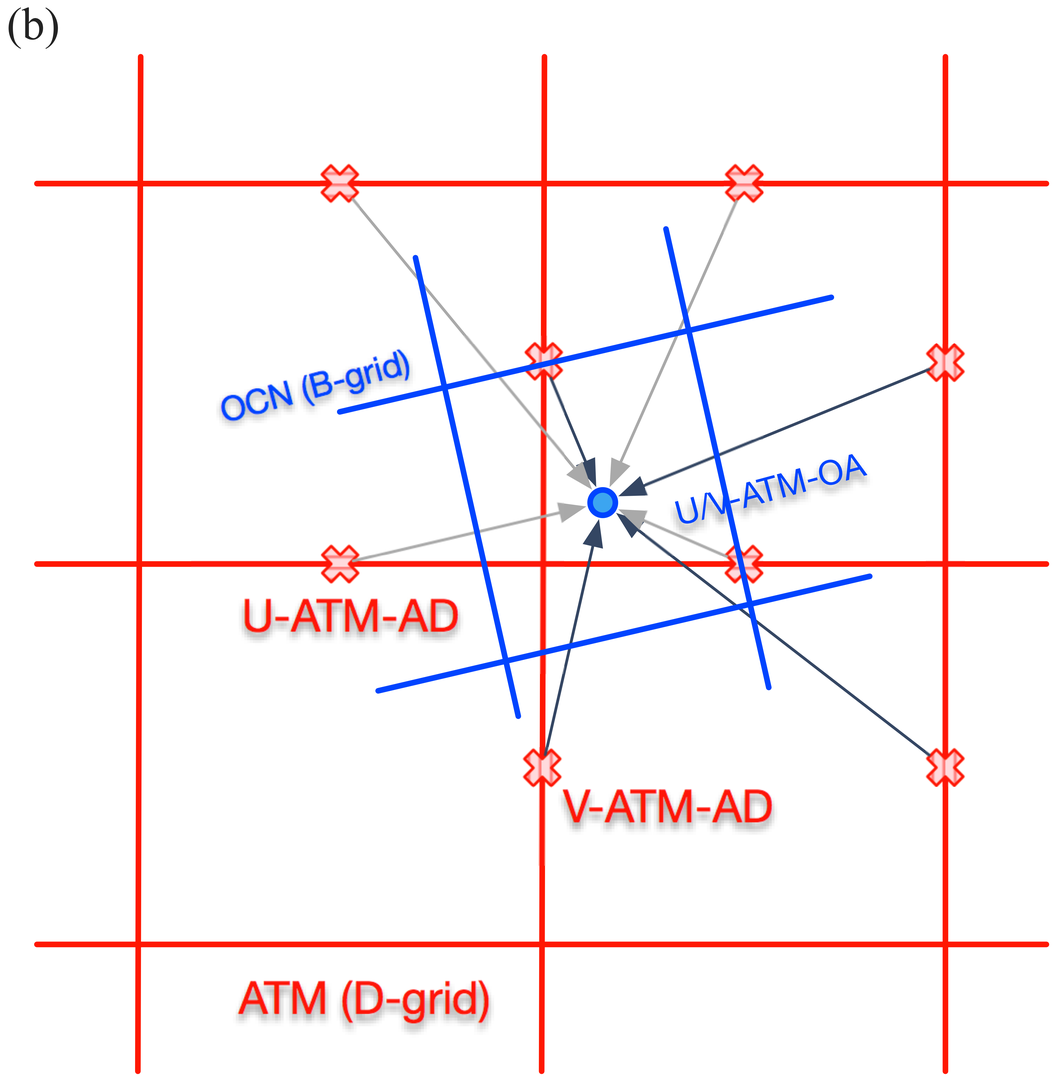
(b)
OCN (B-grid)
U/V-ATM-OA
U-ATM-AD
V-ATM-AD
ATM (D-grid)

Figure3.

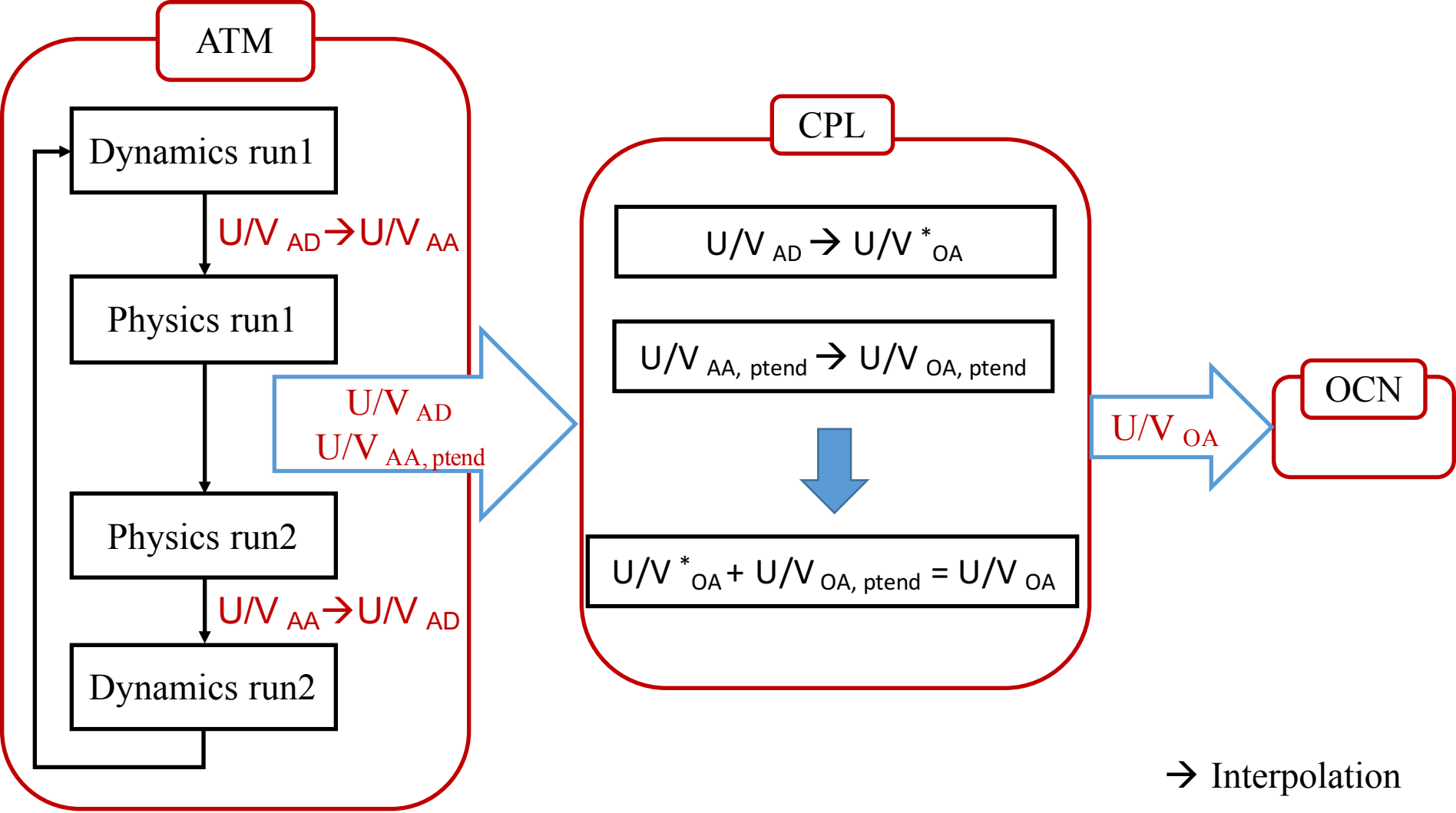
ATM
Dynamics run1
U/V AD → U/V AA
Physics run1
Physics run2
U/V AA → U/V AD
Dynamics run2
U/V AD
U/V AA, ptend
CPL
U/V AD → U/V *OA
U/V AA, ptend → U/V OA, ptend
U/V *OA + U/V OA, ptend = U/V OA
U/V OA
OCN
→ Interpolation

Figure4.

(a)

Mod_cp

SST(°C)

90°N
45°N
0°
45°S
90°S

45°E 90°E 135°E 180° 135°W 90°W 45°W 0°

0 2 4 6 8 10 12 14 16 18 20 22 24 26 28 30 32

(b)

OBS

SST(°C)

90°N
45°N
0°
45°S
90°S

45°E 90°E 135°E 180° 135°W 90°W 45°W 0°

0 2 4 6 8 10 12 14 16 18 20 22 24 26 28 30 32

(c)

Mod_cp-OBS

SST(°C)

90°N
45°N
0°
45°S
90°S

45°E 90°E 135°E 180° 135°W 90°W 45°W 0°

-6 -5 -4 -3 -2 -1 -0.5 0 0.5 1 2 3 4 5 6

(d)

Mod_cp-F09

SST(°C)

90°N
45°N
0°
45°S
90°S

45°E 90°E 135°E 180° 135°W 90°W 45°W 0°

-0.3 -0.2 -0.1 0 0.1 0.2 0.3

Figure5.

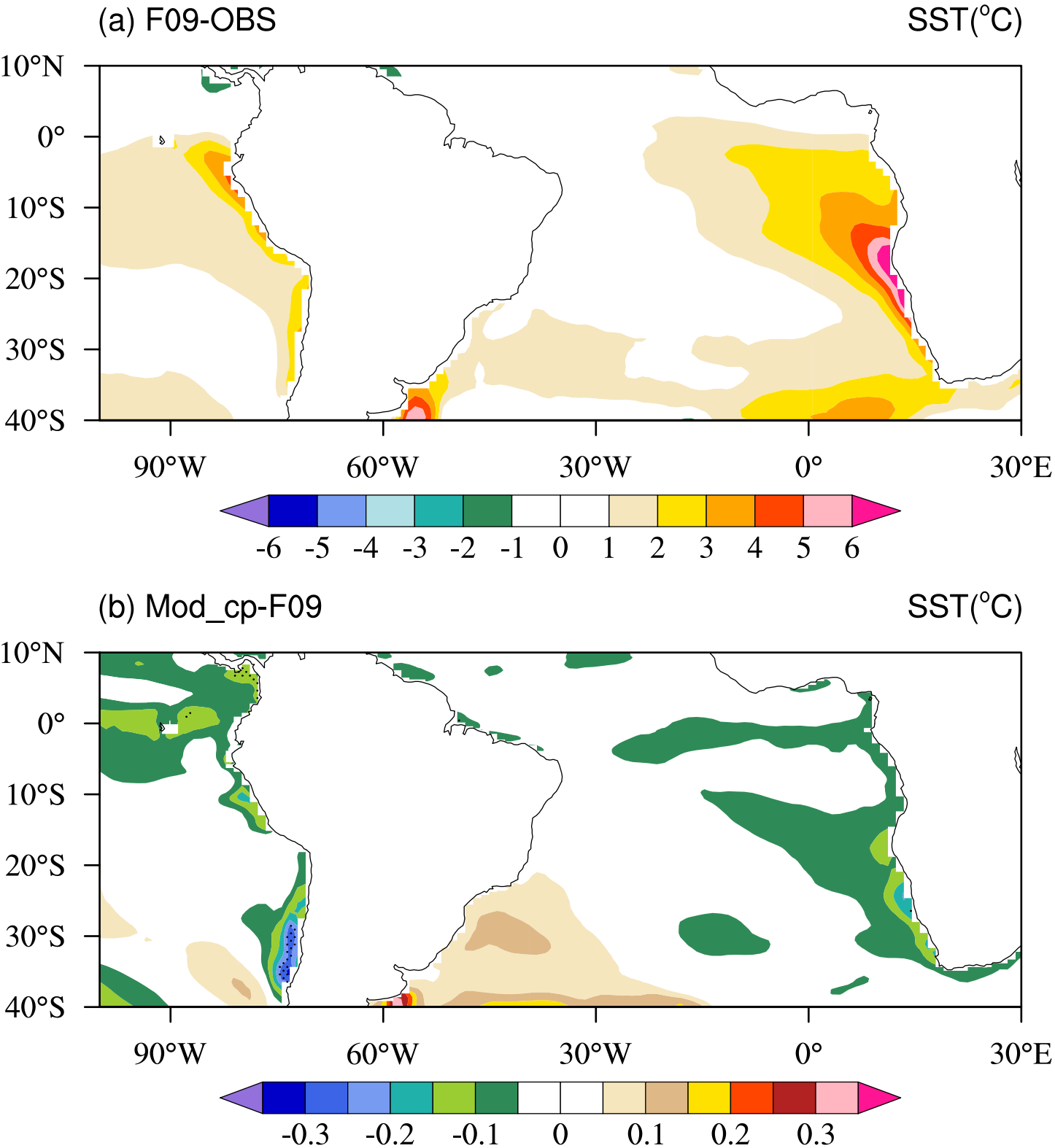
(a) F09-OBS
SST(°C)
10°N
0°
10°S
20°S
30°S
40°S
90°W
60°W
30°W
0°
30°E
-6 -5 -4 -3 -2 -1 0 1 2 3 4 5 6
(b) Mod_cp-F09
SST(°C)
10°N
0°
10°S
20°S
30°S
40°S
90°W
60°W
30°W
0°
30°E
-0.3 -0.2 -0.1 0 0.1 0.2 0.3

Figure6.

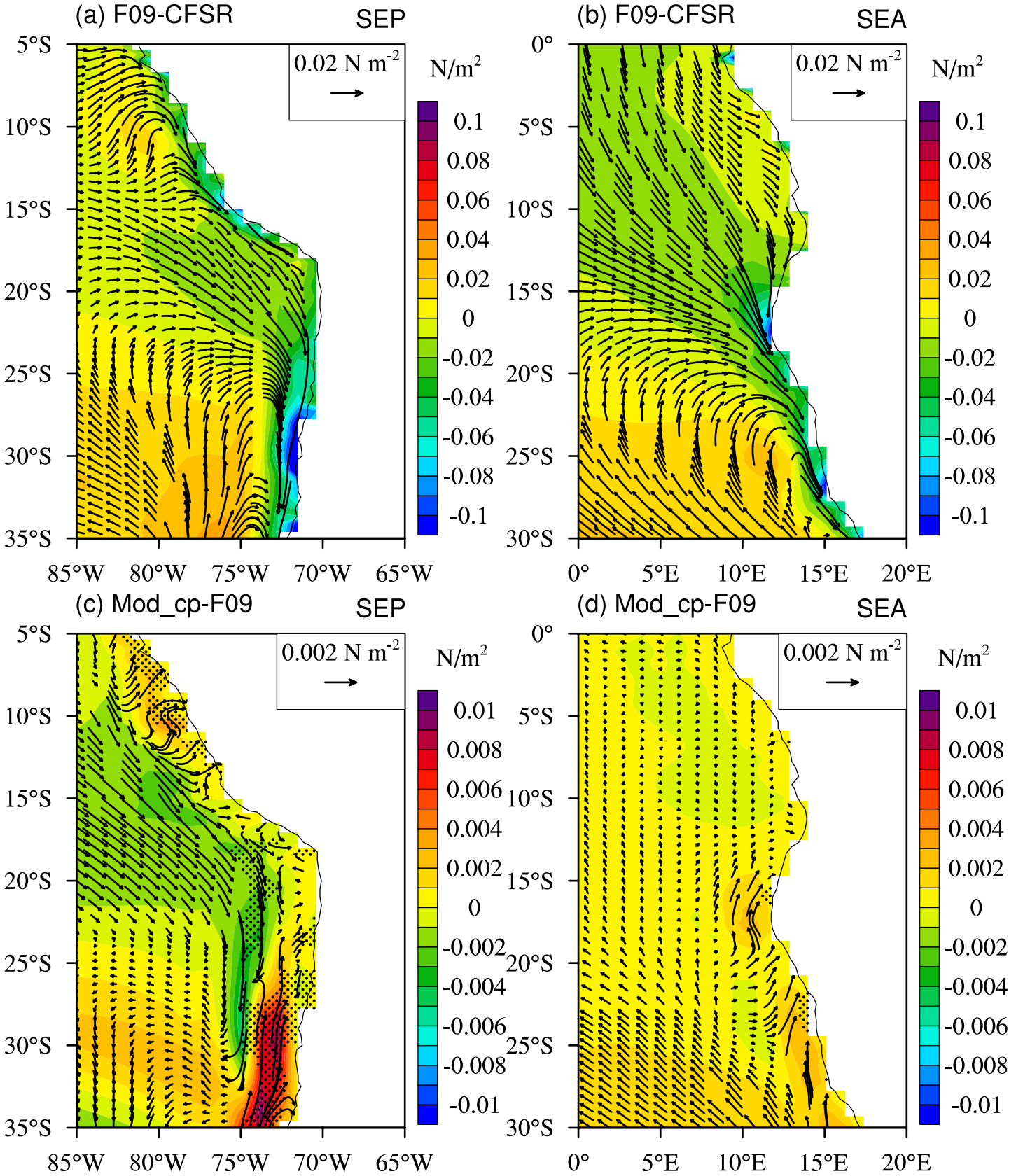
(a) F09-CFSR
SEP
0.02 N m-2
N/m2
0.1
0.08
0.06
0.04
0.02
0
-0.02
-0.04
-0.06
-0.08
-0.1
5°S
10°S
15°S
20°S
25°S
30°S
35°S
85°W
80°W
75°W
70°W
65°W
(b) F09-CFSR
SEA
0.02 N m-2
N/m2
0.1
0.08
0.06
0.04
0.02
0
-0.02
-0.04
-0.06
-0.08
-0.1
0°
5°S
10°S
15°S
20°S
25°S
30°S
0°
5°E
10°E
15°E
20°E
(c) Mod_cp-F09
SEP
0.002 N m-2
N/m2
0.01
0.008
0.006
0.004
0.002
0
-0.002
-0.004
-0.006
-0.008
-0.01
5°S
10°S
15°S
20°S
25°S
30°S
35°S
85°W
80°W
75°W
70°W
65°W
(d) Mod_cp-F09
SEA
0.002 N m-2
N/m2
0.01
0.008
0.006
0.004
0.002
0
-0.002
-0.004
-0.006
-0.008
-0.01
0°
5°S
10°S
15°S
20°S
25°S
30°S
0°
5°E
10°E
15°E
20°E

Figure7.

(a) Mod_cp-F09 VVEL(SEP)

(b) Mod_cp-F09 VVEL(SEA)

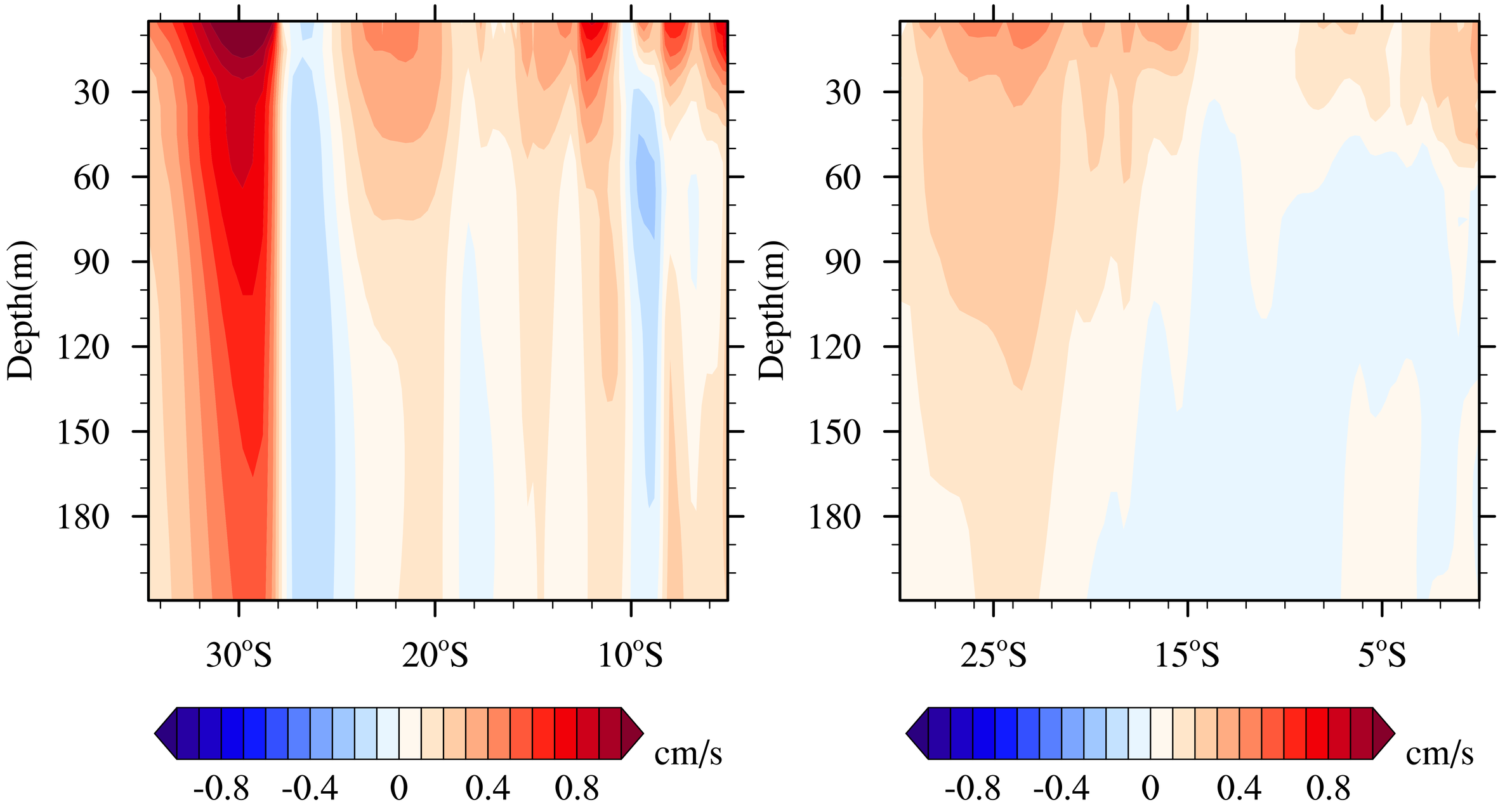

(c) Mod_cp-F09 WVEL(30°S)

(d) Mod_cp-F09 WVEL(17.5°S)

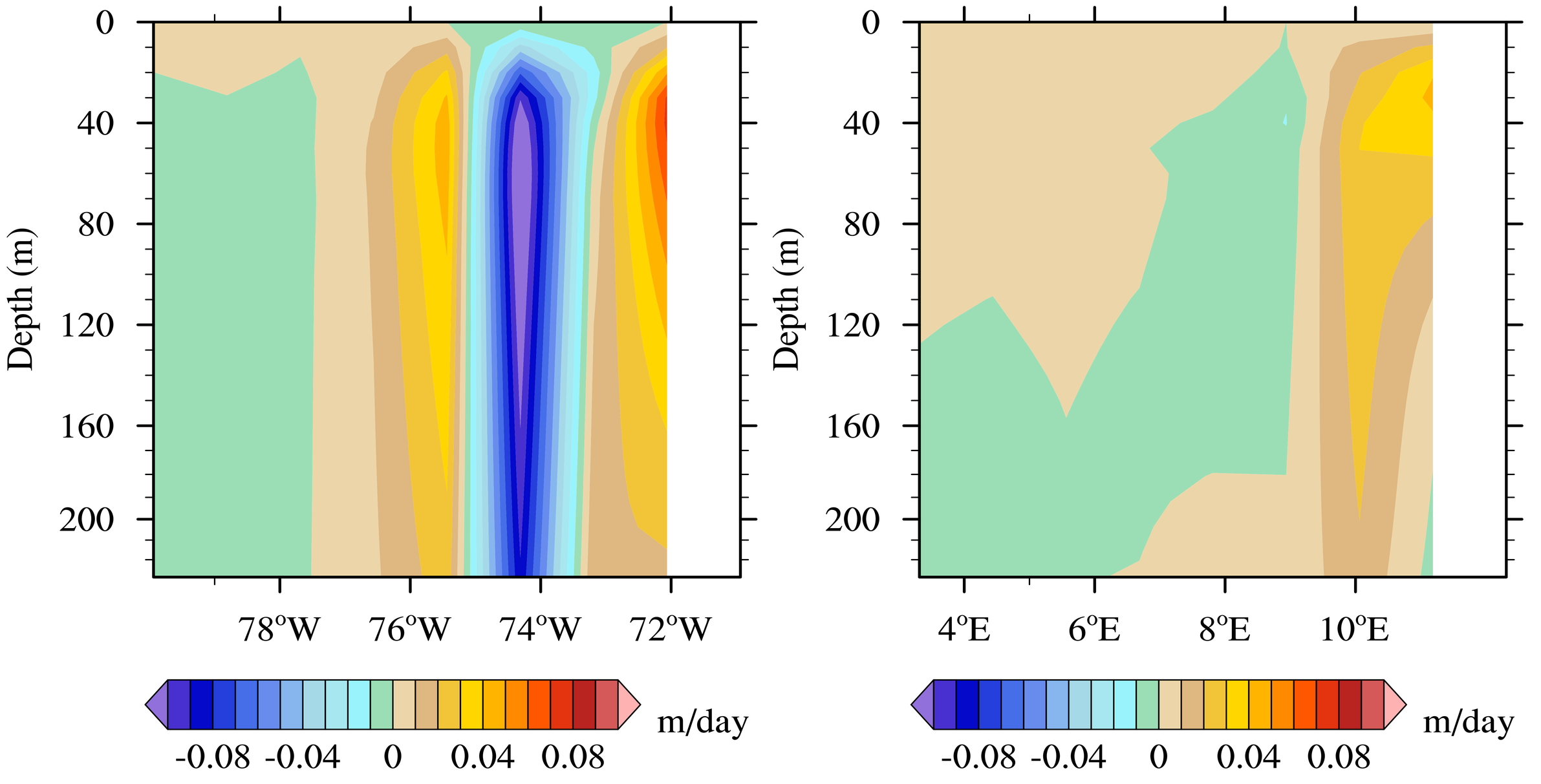

Figure8.

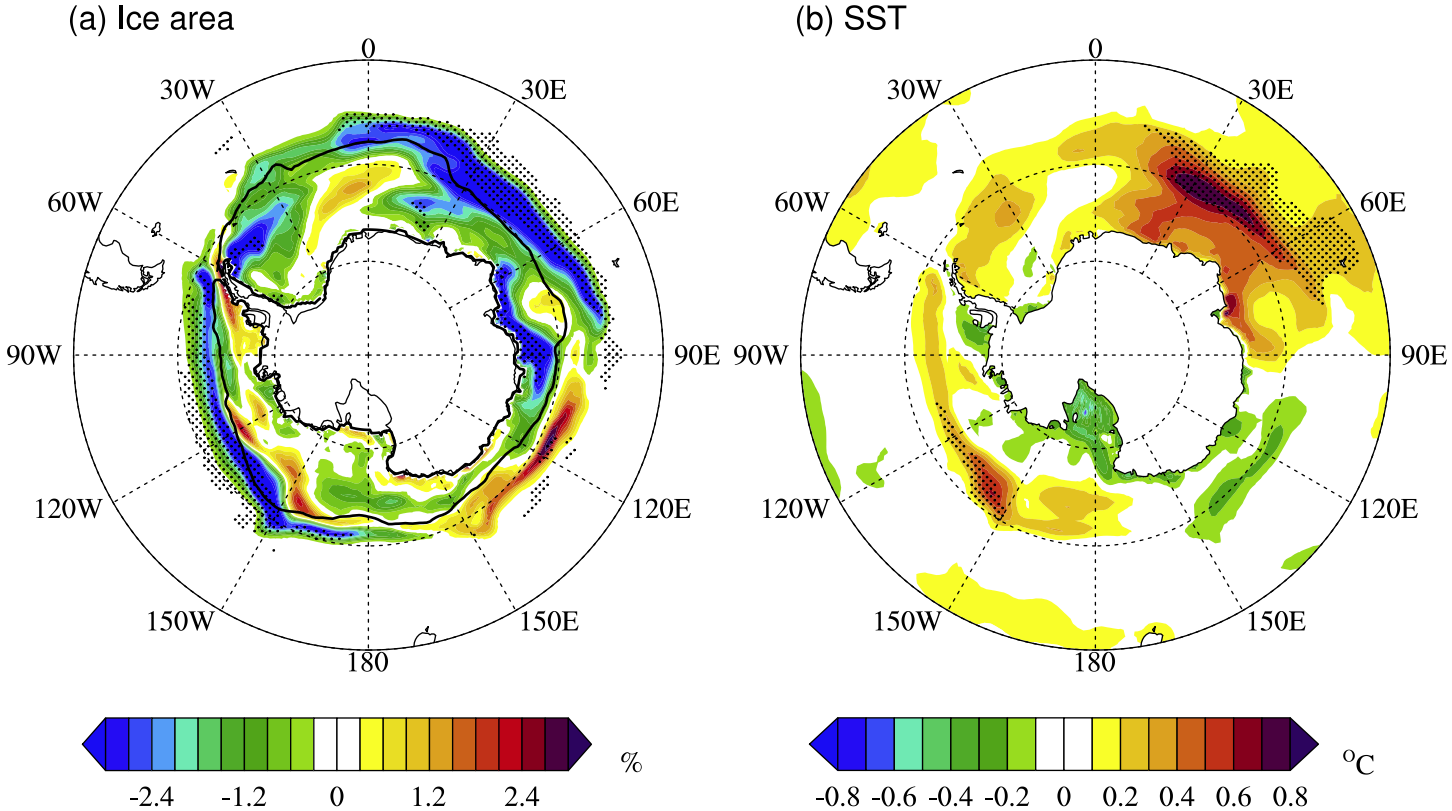
(a) Ice area
0
30W
30E
60W
60E
90W
90E
120W
120E
150W
150E
180
-2.4
-1.2
0
1.2
2.4
%
(b) SST
0
30W
30E
60W
60E
90W
90E
120W
120E
150W
150E
180
-0.8
-0.6
-0.4
-0.2
0
0.2
0.4
0.6
0.8
°C

Figure9.

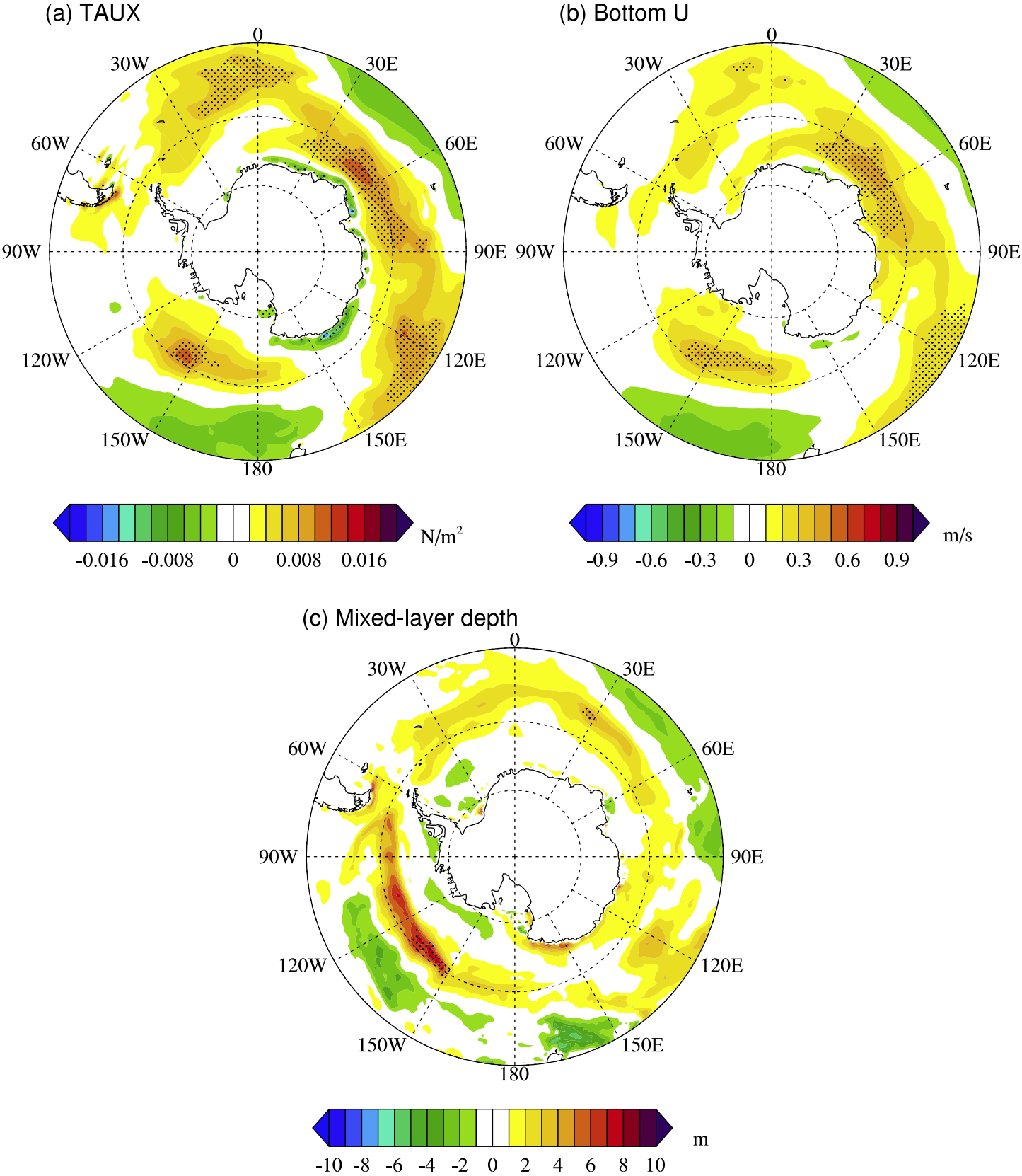
(a) TAUX
0
30W
30E
60W
60E
90W
90E
120W
120E
150W
150E
180
N/m2
-0.016 -0.008 0 0.008 0.016
(b) Bottom U
m/s
-0.9 -0.6 -0.3 0 0.3 0.6 0.9
(c) Mixed-layer depth
m
-10 -8 -6 -4 -2 0 2 4 6 8 10

Figure10.

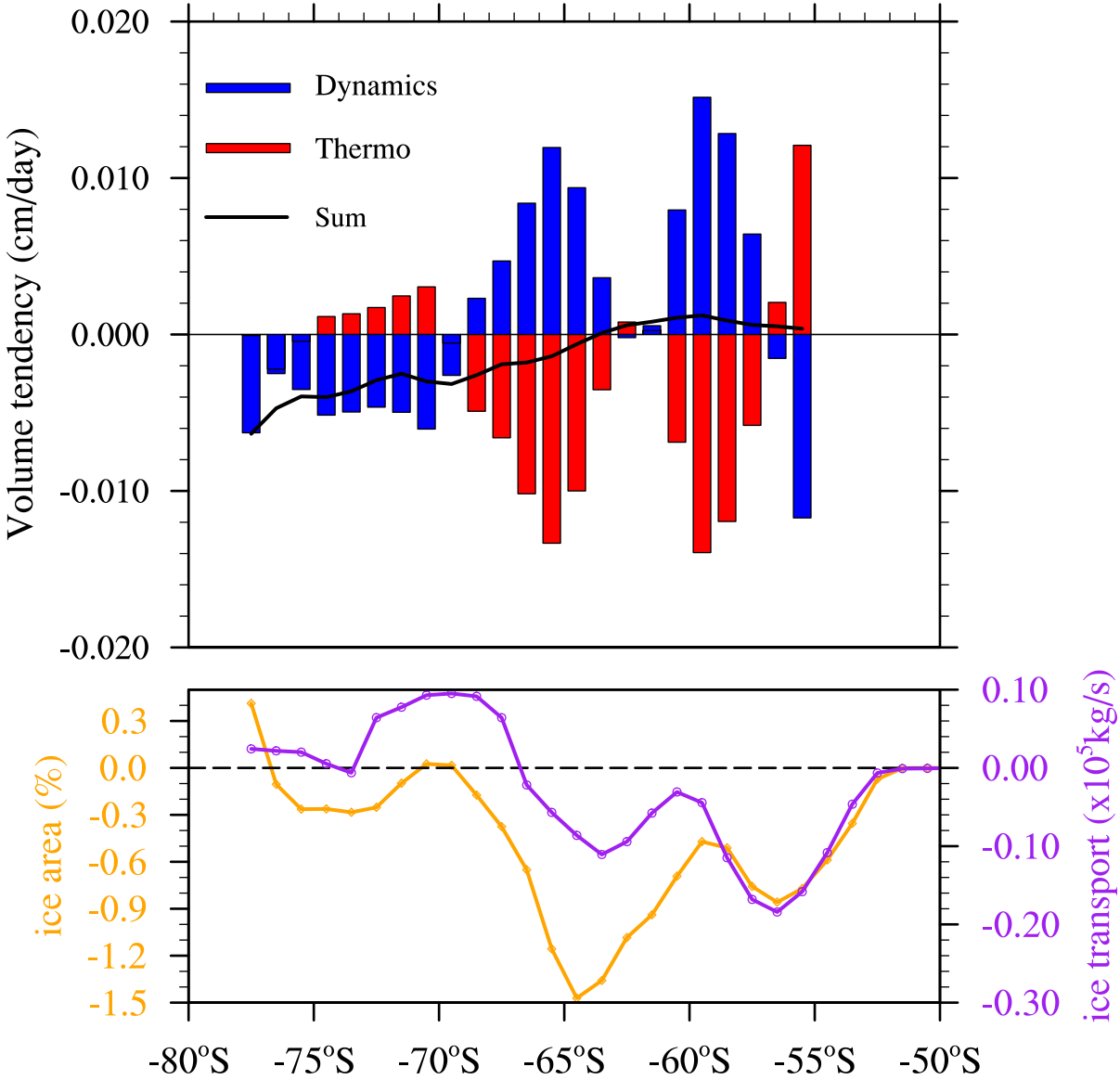
Volume tendency (cm/day)
0.020
0.010
0.000
-0.010
-0.020
Dynamics
Thermo
Sum
ice area (%)
0.3
0.0
-0.3
-0.6
-0.9
-1.2
-1.5
ice transport (x10^{5}kg/s)
0.10
0.00
-0.10
-0.20
-0.30
-80°S
-75°S
-70°S
-65°S
-60°S
-55°S
-50°S